BAMS Article

Observations of Clouds, Aerosols, Precipitation, and Surface Radiation over the Southern Ocean

An Overview of CAPRICORN, MARCUS, MICRE, and SOCRATES

Greg M. McFarquhar, Christopher S. Bretherton, Roger Marchand, Alain Protat, Paul J. DeMott, Simon P. Alexander, Greg C. Roberts, Cynthia H. Twohy, Darin Toohey, Steve Siems, Yi Huang, Robert Wood, Robert M. Rauber, Sonia Lasher-Trapp, Jorgen Jensen, Jeffrey L. Stith, Jay Mace, Junshik Um, Emma Järvinen, Martin Schnaiter, Andrew Gettelman, Kevin J. Sanchez, Christina S. McCluskey, Lynn M. Russell, Isabel L. McCoy, Rachel L. Atlas, Charles G. Bardeen, Kathryn A. Moore, Thomas C. J. Hill, Ruhi S. Humphries, Melita D. Keywood, Zoran Ristovski, Luke Cravigan, Robyn Schofield, Chris Fairall, Marc D. Mallet, Sonia M. Kreidenweis, Bryan Rainwater, John D'Alessandro, Yang Wang, Wei Wu, Georges Saliba, Ezra J. T. Levin, Saisai Ding, Francisco Lang, Son C. H. Truong, Cory Wolff, Julie Haggerty, Mike J. Harvey, Andrew R. Klekociuk, and Adrian McDonald

ABSTRACT: Weather and climate models are challenged by uncertainties and biases in simulating Southern Ocean (SO) radiative fluxes that trace to a poor understanding of cloud, aerosol, precipitation, and radiative processes, and their interactions. Projects between 2016 and 2018 used in situ probes, radar, lidar, and other instruments to make comprehensive measurements of thermodynamics, surface radiation, cloud, precipitation, aerosol, cloud condensation nuclei (CCN), and ice nucleating particles over the SO cold waters, and in ubiquitous liquid and mixed-phase clouds common to this pristine environment. Data including soundings were collected from the NSF–NCAR G-V aircraft flying north–south gradients south of Tasmania, at Macquarie Island, and on the R/V *Investigator* and RSV *Aurora Australis*. Synergistically these data characterize boundary layer and free troposphere environmental properties, and represent the most comprehensive data of this type available south of the oceanic polar front, in the cold sector of SO cyclones, and across seasons. Results show largely pristine environments with numerous small and few large aerosols above cloud, suggesting new particle formation and limited long-range transport from continents, high variability in CCN and cloud droplet concentrations, and ubiquitous supercooled water in thin, multilayered clouds, often with small-scale generating cells near cloud top. These observations demonstrate how cloud properties depend on aerosols while highlighting the importance of dynamics and turbulence that likely drive heterogeneity of cloud phase. Satellite retrievals confirmed low clouds were responsible for radiation biases. The combination of models and observations is examining how aerosols and meteorology couple to control SO water and energy budgets.

KEYWORDS: Southern Ocean; Cloud microphysics; Cloud radiative effects; Cloud water/phase; Radiation budgets; Aerosol-cloud interaction

https://doi.org/10.1175/BAMS-D-20-0132.1
Corresponding author: Greg M. McFarquhar, mcfarq@ou.edu
Supplemental material: https://doi.org/10.1175/BAMS-D-20-0132.2

In final form 30 September 2020

AFFILIATIONS: McFarquhar and D'Alessandro—Cooperative Institute for Mesoscale Meteorological Studies, and School of Meteorology, University of Oklahoma, Norman, Oklahoma; **Bretherton, Marchand, Wood, McCoy, and Atlas**—Department of Atmospheric Sciences, University of Washington, Seattle, Washington; **Protat**—Australian Bureau of Meteorology, Melbourne, Victoria, and Australian Antarctic Programme Partnership, Institute for Marine and Antarctic Science, University of Tasmania, Hobart, Tasmania, Australia; **DeMott, Moore, Hill, and Kreidenweis**—Department of Atmospheric Science, Colorado State University, Fort Collins, Colorado; **Alexander and Klekociuk**—Australian Antarctic Division, and Australian Antarctic Programme Partnership, Institute for Marine and Antarctic Science, University of Tasmania, Hobart, Tasmania, Australia; **Roberts**—Scripps Institution of Oceanography, La Jolla, California, and Centre National de Recherches Météorologiques, UMR3589, Toulouse, France; **Twohy**—NorthWest Research Associates, Redmond, Washington, and Scripps Institution of Oceanography, La Jolla, California; **Toohey and Rainwater**—Department of Atmospheric and Oceanic Sciences, University of Colorado Boulder, Boulder, Colorado; **Siems, Lang, and Truong**—School of Earth, Atmosphere and Environment, Monash University, Melbourne, Victoria, Australia; **Huang and Schofield**—School of Earth Sciences, University of Melbourne, Melbourne, Victoria, Australia; **Rauber and Lasher-Trapp**—Department of Atmospheric Sciences, University of Illinois at Urbana–Champaign, Urbana, Illinois; **Jensen, Stith, Gettelman, McCluskey, Bardeen, Wolff, and Haggerty**—National Center for Atmospheric Research, Boulder, Colorado; **Mace**—University of Utah, Salt Lake City, Utah; **Um**—Cooperative Institute for Mesoscale Meteorological Studies, University of Oklahoma, Norman, Oklahoma, and Department of Atmospheric Sciences, Pusan National University, Busan, South Korea; **Järvinen**—National Center for Atmospheric Research, Boulder, Colorado, and Karlsruhe Institute of Technology, Karlsruhe, Germany; **Schnaiter**—Karlsruhe Institute of Technology, Karlsruhe, Germany; **Sanchez, Russell, and Saliba**—Scripps Institution of Oceanography, La Jolla, California; **Humphries and Keywood**—Climate Science Centre, Oceans and Atmosphere, CSIRO, Melbourne, Victoria, Australia; **Ristovski and Cravigan**—School of Earth and Atmospheric Sciences, Queensland University of Technology, Brisbane, Queensland, Australia; **Fairall**—NOAA, Boulder, Colorado; **Mallet**—Australian Antarctic Programme Partnership, Institute for Marine and Antarctic Science, University of Tasmania, Hobart, Tasmania, Australia; **Wang**—Cooperative Institute for Mesoscale Meteorological Studies, University of Oklahoma, Norman, Oklahoma, and Beijing Normal University, Beijing, China; **Wu**—Cooperative Institute for Mesoscale Meteorological Studies, University of Oklahoma, Norman, Oklahoma; **Levin**—Department of Atmospheric Science, Colorado State University, Fort Collins, and Handix Scientific, Boulder, Colorado; **Saisai Ding**—Peking University, Beijing, China; **Harvey**—National Institute of Water and Atmospheric Research, Wellington, New Zealand; **McDonald**—Gateway Antarctica, and School of Physical and Chemical Sciences, University of Canterbury, Christchurch, New Zealand

The Southern Ocean (SO) surrounding Antarctica and consisting of parts of the southern Atlantic, Pacific and Indian Oceans, is one of the cloudiest places on Earth. The fractional cover of low clouds (below 3-km altitude) prevalent in the warm and cold sectors of frequent extratropical cyclones reaches nearly 80% year-round (Mace et al. 2009; IPCC 2013). Relative to more easily sampled locations, there is a dearth of in situ observations of aerosols, clouds, and precipitation over the SO, especially south of 60°S. This makes it difficult to evaluate remote sensing retrieval products. General circulation models (GCMs) have difficulty with simulating the present-day aerosol, cloud coverage and cloud phase over the SO, with implications for anthropogenic aerosol impacts and cloud feedbacks on climate (e.g., Trenberth and Fasullo 2010; Tan et al. 2016), two key uncertainties in interpreting the historical climate record and projecting future climate change.

Numerical weather prediction (NWP) and GCMs have struggled to correctly simulate the radiative budget over the SO due to low cloud biases. Most Coupled Model Intercomparison Project phase 5 (CMIP5) models predict too much shortwave (SW) radiation absorbed over the SO region (Bodas-Salcedo et al. 2014, 2016; Naud et al. 2014), with impacts on ocean temperature, the Southern Hemisphere (SH) jet (Ceppi et al. 2014), Antarctic sea ice trends

(Flato et al. 2013) and tropical rainfall (Hwang and Frierson 2013). Comparisons with satellite data indicate that model radiative biases are due primarily to a lack of low- and midlevel clouds in the cold sectors of cyclones (e.g., Flato et al. 2013; Bodas-Salcedo et al. 2014). It was hypothesized on the basis of limited observations, mainly from satellites, that GCMs might be glaciating what are in reality persistent supercooled liquid clouds. Indeed, GCM simulations in which convective parameterizations have been forced to produce greater amounts of supercooled liquid water (SLW) have reduced SW biases (Kay et al. 2016).

A related motivating issue is the apparent paucity of ice nucleating particles (INPs) over the SO (Bigg 1973; Burrows et al. 2013), due to it being far removed from any continental air sources; INP parameterizations are based mostly on Northern Hemisphere (NH) observations. Satellite retrievals of cloud-top phase indicate that SLW is more prevalent over the SO than at equivalent latitudes in the NH (Choi et al. 2010; Hu et al. 2010; Morrison et al. 2011). This could be because SO supercooled clouds are starved for INPs, as hypothesized by Kanitz et al. (2011) and Vergara-Temprado et al. (2018).

A final overarching question is how droplet concentrations are regulated in SO boundary layer (BL) clouds in a synoptically active environment with high winds over a biologically productive ocean. The SO is a biologically unique marine aerosol environment, its pristine nature is as close to preindustrial conditions as exists on Earth, and thus represents a natural laboratory to study anthropogenic aerosol indirect radiative forcing (Carslaw et al. 2013; Ghan et al. 2013). Hoose et al. (2009) showed that GCMs with prognostic aerosols tended to simulate SO clouds with too few droplets compared to satellite observations, making them overly susceptible to human aerosol perturbations. One hypothesis is that these models underestimate marine biogenic production of cloud condensation nuclei (CCN). Satellite retrievals and some previous field observations show the SO has a strong summertime maximum in cloud droplet concentration N_c (Boers et al. 1996, 1998), CCN (Ayers and Gras 1991), and aerosol concentrations N_a (Sciare et al. 2009) correlated with phytoplankton productivity. Quinn et al. (2017) found that except for the high southern latitudes, sea spray contributes less than 30% to the total CCN. However, observations in the Aerosol Characterization Experiment 1 (ACE-1) campaign suggested that copious sulfate aerosols can be produced in the outflow of shallow precipitating cumulus clouds from nucleation of marine biogenic gases (Hudson et al. 1998; Clarke et al. 1998; Russell et al. 1998).

Thus, there is a clear need for observations to help better model the natural aerosol life cycle and mixed-phase BL cloud over the SO. Prior to the campaigns described here, cloud and aerosol measurements over the SO included those listed in Table 1. But, further observations on cloud and aerosol concentrations over cold waters poleward of 60°S are critical for understanding cloud processes over the SO. To understand the transition of aerosols to CCN over the remote oceans, it is necessary to quantify particle sources and sinks as well as processes related to their aging, including the role of new particle formation in the free troposphere, generation from breaking waves over the ocean, generation of biogenic particles from gas phase oceanic emissions, the role of precipitation scavenging, and the effects of updrafts and dynamics on clouds.

Climate model evaluation, and much current knowledge of SO clouds, aerosols, precipitation, and surface radiation properties is based on satellite retrievals. Satellite studies have found that cloud-top SLW is more frequent over the SO (Hu et al. 2010; Choi et al. 2010; Huang et al. 2012a,b; Kanitz et al. 2011; Morrison et al. 2011; Protat et al. 2014; Huang et al. 2015a, 2016) and Antarctic (Grosvenor et al. 2012) than over the NH, but there are significant variations between satellite retrieval products in the frequency of cloud-top SLW (Delanoë and Hogan 2010; Huang et al. 2015a) and these retrievals tell us little about the phase of condensate below cloud top. However, potential errors in cloud retrievals, particularly those related to large solar zenith angles (Grosvenor and Wood 2014) and

Table 1. Previous field campaigns and data collection activities over the SO.

Campaign	Description	Reference
Aerosol Characterization Experiment 1 (ACE-1)	Sea spray aerosol, vertical aerosol profiles and fluxes	Bates et al. (1998a,b), Clarke et al. (1998), Weber et al. (1998), Russell et al. (1998)
HIAPER Pole-to-Pole Observations (HIPPO)	Four transects sampling clouds and aerosols south of Macquarie Island	Wofsy et al. (2011), Chubb et al. (2013, 2016)
SIPEX II	Aerosol number concentrations across polar front	Humphries (2015, 2016)
O_2/N_2 Ratio and CO_2 Airborne Southern Ocean Study (ORCAS)	Limited cloud sampling	Stephens et al. (2018), D'Alessandro et al. (2019)
Observations near Tasmania	Observations in wintertime low-altitude clouds over open ocean near Tasmania	Ahn et al. (2017), Huang et al. (2015b, 2017)
Cape Grim observations	CCN observations at Cape Grim (41°S, 145°E)	Gras and Keywood (2017)
Southern Ocean Cloud Experiment (SOCEX)	Aerosol optical depth and composition, clouds	Sciare et al. (2009), Boers et al. (1996, 1998)
Recent ship-based observations (separate from campaigns described here)	Limited set of cloud radiation and aerosol properties south of 60°S and circumpolar quantification of aerosol properties	Kuma et al. (2020), Klekociuk et al. (2020a), Hartery et al. (2020), Schmale et al. (2019)

three-dimensional effects (Wolters et al. 2010; Zeng et al. 2012; Cho et al. 2015) remain a concern. Additional ground-based and airborne remote sensing, and airborne in situ measurements, are therefore needed to evaluate satellite retrievals.

A 2014 community workshop at the University of Washington discussed these issues, recognizing the need for a large international multiagency effort to improve the understanding of clouds, aerosols, precipitation and their interactions over the SO (Marchand et al. 2014). The workshop served as a motivation for the proposals of separate, but integrated, projects to various funding agencies in the United States and Australia. These four collaborative projects were 1) the Clouds Aerosols Precipitation Radiation and atmospheric Composition over the Southern Ocean (CAPRICORN) I and II research voyages of the Research Vessel (R/V) *Investigator*, led by the Australian Bureau of Meteorology (BoM), that made extensive in situ and remote sensing measurements in 2016 and 2018, respectively; 2) the 2017–18 Measurements of Aerosols, Radiation and Clouds over the Southern Ocean (MARCUS) project, during which the United States Department of Energy (DOE) Atmospheric Radiation Measurement (ARM) Program Mobile Facility 2 (AMF2) was deployed on the Australian icebreaker Research Supply Vessel (RSV) *Aurora Australis* (*AA*) as it made resupply voyages to Australian Antarctic bases; 3) the 2016–18 Macquarie Island Cloud Radiation Experiment (MICRE) acquiring surface in situ and remote sensing observations using equipment from DOE ARM, the BoM, and the Australian Antarctic Division (AAD); and 4) the 2018 Southern Ocean Cloud Radiation and Aerosol Transport Experimental Study (SOCRATES) using the NSF–NCAR G-V aircraft to sample clouds, aerosols, and precipitation from Hobart, Australia, to within approximately 650 km of the Antarctic coast. Although each project was a separate effort and no formal steering committee coordinated the projects, many investigators served on the advisory board of several of the projects and there was much collaboration between the campaigns. There was one integrated planning workshop (2017 Boulder) and two integrated data workshops after the completion of the projects (2018 Boulder, 2019 Hobart). Data have been freely exchanged among participants, and a special collection of papers in the *Journal of Geophysical Research/Geophysical Research Letters* covering all four projects has been established and is expected to grow substantially over the next few years. This collaboration is essential to maximize the projects' impacts. Synergistically these data provide the best available measurements of the

BL and free troposphere structure, together with vertical distributions of liquid and mixed-phase clouds and aerosols properties, over cold SO waters where SLW and mixed-phase BL clouds are frequent.

Overview of field campaigns

In this section, the campaigns are introduced, detailing the scientific objectives, the time period of the observations, the instruments and platforms used to acquire the observations, the manner in which the observations were obtained, and a broad overview of the meteorological conditions sampled. The majority of the observations was obtained in a north–south curtain extending from Hobart, Australia, to the Antarctic coast in the Australasian sector of the SO. Figure 1 shows the ship tracks from CAPRICORN I, II and MARCUS, as well as the G-V flight tracks during SOCRATES and the location of the ground-observing site at Macquarie Island during MICRE.

MICRE. The DOE ARM program, the AAD and the BoM collaborated in deploying ground instrumentation to Macquarie Island between March 2016 and March 2018. Macquarie Island is located at 54.5°S, 158.9°E (north of the oceanic polar front, Fig. 1) and has a small research station operated by the AAD that is staffed year-round, in part by BoM. The station supports a variety of research activities and includes a long history of surface weather and radiosonde observations (Hande et al. 2012; Wang et al. 2015).

The primary objective of MICRE was to collect surface-based observations of radiation, precipitation, BL clouds, and aerosol properties in order to evaluate satellite datasets and to improve knowledge of diurnal and seasonal variations, especially with regards to the vertical structure of BL clouds. Instrumentation deployed during MICRE is listed in Table ES1 (in the online supplement; https://doi.org/10.1175/BAMS-D-20-0132.2), along with time periods for which high-quality observations are available for each instrument in Table ES2. The data

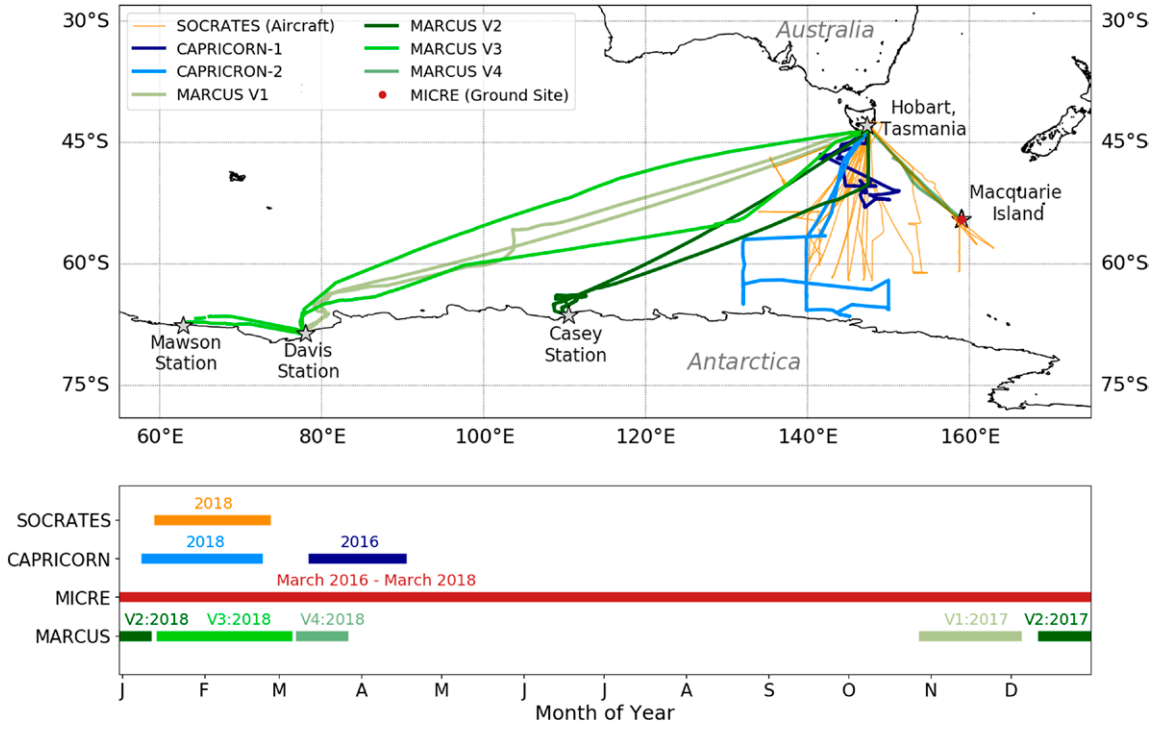

Fig. 1. (top) Ship tracks from CAPRICORN I (dark blue), CAPRICORN II (light blue), and MARCUS voyages (green colors), as well as the SOCRATES G-V flight tracks (orange) and the location of the ground-observing site at Macquarie Island during MICRE (red). The locations of Mawson, Davis, and Casey stations are also shown (gray stars). (bottom) The years and seasons corresponding to each campaign.

include (i) passive surface radiation (solar, longwave, microwave); (ii) surface precipitation rain rates, types and particle sizes; (iii) cloud radar reflectivity and Doppler velocity profiles, ceilometer and lidar backscatter (including depolarization) measurements (that provide information on cloud occurrence, cloud-base and cloud-top height, precipitation particle size and phase, and some vertically resolved aerosol optical properties in cloud-free conditions); (iv) ground-based number concentrations of total aerosol and CCN; and (v) ground-based INP number concentration and type (via filter sample analyses).

CAPRICORN. CAPRICORN was a sea-based field study using the Australian Marine National Facility (MNF) R/V *Investigator*, designed to better understand interrelated aerosol–cloud–precipitation–radiation processes responsible for surface SW radiation biases in global models and discrepancies between satellite rainfall measurements south of 40°S (e.g., Skofronick-Jackson et al. 2017; Protat et al. 2019a,b). The objectives were to (i) characterize cloud, aerosol, and precipitation properties, BL structure, biological production and cycling of dimethyl sulfide (DMS) in the upper ocean, atmospheric composition, and surface energy budget, as well as their latitudinal variability; (ii) evaluate and improve satellite products [with a focus on the NASA A-Train and NASA/JAXA Global Precipitation Measurement (GPM) mission cloud and precipitation products, and surface heat flux products]; and (iii) evaluate and improve the representation of these properties in the regional and global versions of the Australian Community Climate and Earth-System Simulator (ACCESS) model (Puri et al. 2013). A second voyage, CAPRICORN II, occurred simultaneously within the same overall region (south of Australia) as SOCRATES, and included four flights where the NCAR G-V aircraft passed over or near the R/V *Investigator*.

CAPRICORN I, held 13 March–15 April 2016 south of Tasmania, used the instruments listed in Table ES3. All instruments operated near 100% of the time, and characterized the basic atmospheric state (~1 radiosonde per day), vertical cloud structure, including integrated liquid water and water vapor contents, cloud phase, and microphysical properties (based on cloud radar, lidar, and microwave radiometer measurements), and rainfall rates and drop size distributions (from disdrometer and micro rain radar measurements). The aerosol size distributions, morphologies and compositions, size-resolved chemical compositions and hygroscopic growth factors, cloud nuclei, CCN and INP concentrations, and some gaseous atmospheric compositions including DMS and VOCs, were measured. Bioaerosol size distributions, air–sea bulk and turbulent fluxes and surface energy budgets, and subsurface oceanic properties were also measured. Three *CloudSat–CALIPSO* overpasses were successfully intersected by the ship. The online supplement contains more details about the CAPRICORN I voyage, including dates and locations of five cases when the R/V *Investigator* was in the cold sector of major cold fronts in Table ES4.

The main limitation of CAPRICORN I was its latitude span, with no measurements collected south of 55°S (Figs. 1 and 2), and the period (late austral summer–early fall, thereby not providing observations in the summer season where the largest surface radiation bias is found in GCMs). This motivated CAPRICORN II, where the same comprehensive set of data as CAPRICORN I was collected south of 55°S during summer. CAPRICORN II was held from 11 January to 21 February 2018, in combination with a major oceanographic project on the R/V *Investigator* aimed at quantifying changes in water properties and circulation of the SO, and measuring distributions of trace metals and isotopes in the SO and the physical, chemical, and biological processes controlling their evolving distributions. The objectives were similar to CAPRICORN I, with the additional aim to collect precipitation measurements within the swath of the GPM dual-frequency radar. The instrumentation was similar (Table ES5), with notable additions of the C-band dual-polarization Doppler radar (which did not operate during CAPRICORN I) and the NSF-funded contributions as part of SOCRATES that included radiosonde launches every 6 h, remote sensing instruments, and INP and bioaerosol measurements.

More details about the voyage and cloud types sampled are included in the online supplement. Seventeen cases of collocated GPM observations were collected with rain, snow, and mixed-phase precipitation (Table ES6). The number of identified cold sectors and cold fronts traversed by the R/V *Investigator* during CAPRICORN II are listed in Table ES7.

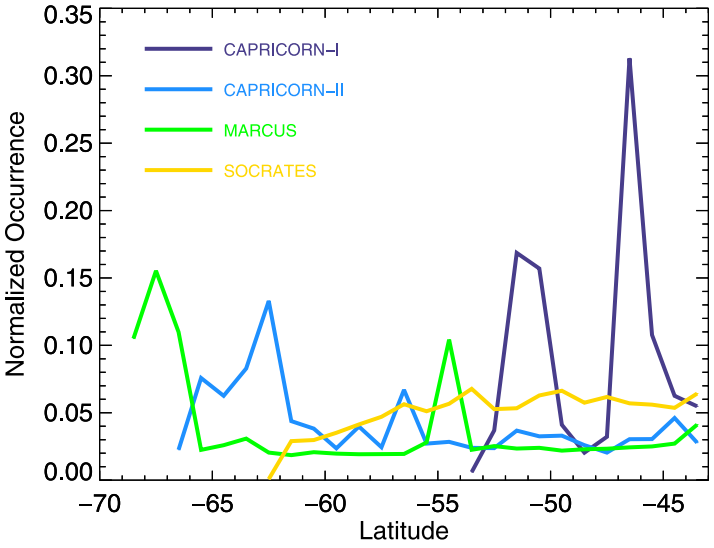

Fig. 2. Normalized frequency of sampling in each 1° latitude bin sampled during MARCUS (green), CAPRICORN I (dark blue), CAPRICORN II (light blue), and SOCRATES (yellow). These are based on the following total number of minutes that each campaign sampled south of 43°S: SOCRATES: 6,319 min; MARCUS: 182,470 min; CAPRICORN I: 44,408 min; CAPRICORN II: 60,060 min.

MARCUS. During MARCUS the DOE AMF2 instrument package, including the Aerosol Observing System (AOS) was installed on the *AA* as it made routine transits between Hobart, Australia and the Australian Antarctic stations of Mawson, Davis, and Casey, as well as Macquarie Island between 21 October 2017 and 23 March 2018. MARCUS observations enhance the CAPRICORN observations in that they were collected over a 5-month period centered upon the austral summer, allowing transitions from spring to fall to be observed across the 80 days of the MARCUS voyages. Because the data were collected during resupply voyages, the science team had no control on the timing of the voyages, nor could specific cloud types be targeted. Thus, a range of synoptic settings was sampled, providing knowledge of temperature-dependent distributions of cloud properties under a variety of aerosol and cloud conditions.

Specific objectives proposed for MARCUS were to 1) understand the synoptically varying vertical structure of SO BL clouds and aerosols; 2) quantify sources and sinks of SO CCN and INPs, including the role of local biogenic sources over spring, summer and fall; 3) quantify mechanisms controlling SLW and mixed-phase clouds; and 4) advance retrievals of clouds, precipitation and aerosols over the SO. Parameterization development and model evaluation requirements were integrated in MARCUS's design so that systematic confrontation and improvement of GCMs and NWP is possible. Instrumentation deployed during MARCUS, listed in Table ES8, included active and passive remote sensing instrumentation, in situ measurements of aerosols, bioaerosols, and INPs, trace gas measurements, and meteorological measurements including 6-hourly radiosonde launches, rain gauges, and disdrometers. The conditions sampled are listed in the online supplement including passages through cold fronts (Table ES9).

SOCRATES. SOCRATES used the NSF–NCAR G-V aircraft to sample clouds, aerosols and precipitation along (primarily) north–south transects south of Hobart, Australia, reaching as far south as 62°S, from 15 January to 26 February 2018. The G-V made in situ measurements within the BL and free troposphere, and included remotely sensed measurements using a cloud radar and lidar. The G-V flight tracks, shown in Fig. 1, were designed to target the cold sectors of cyclones where models have the most trouble producing SLW, and thus were not the same for each day.

The overarching objectives of SOCRATES were similar to those of MARCUS, MICRE and CAPRICORN. In particular, the G-V was tasked to obtain a dataset characterizing the structure of the MBL and free troposphere over the SO, including observations of the vertical distribution

and properties of clouds and aerosols, including CCN and INPs, so that possible mechanisms to explain the excessive absorbed SW radiation in models could be tested. The instruments and flight paths were designed to gather statistics on aerosols and clouds as a function of latitude, and included measurements over both the R/V *Investigator* during CAPRICORN II and Macquarie Island as explained in the online supplement. Table ES10 lists the instrumentation installed on the G-V including in situ cloud and aerosol probes and remote sensing devices. The online supplement also provides information about the sampling strategy that was used to execute flights collecting both in situ and remote sensing data along with a list of all the research flights (RFs) in Table ES11.

Figure 2 shows the normalized fraction of observations made at each latitude during the four campaigns. Apart from time spent at the Australian Antarctic stations and Macquarie Island for resupplying during MARCUS, there is an even sampling of latitudes during both CAPRICORN II and MARCUS. Both the R/V *Investigator* and RSV *Aurora Australis* spent a large time south of 60°S, providing a very rare and invaluable set of data over cold waters poleward of the oceanic polar front. MARCUS data are unique because they provide observations over the sea ice and cover more of a seasonal cycle (October–March) than CAPRICORN II, whereas CAPRICORN I and II included more thorough aerosol, oceanographic, and surface energy budget measurements to put cloud observations in context, and MICRE provides the longest seasonal cycle at a single location. SOCRATES provides the in situ observations that are critical for process studies and evaluation of remote sensing retrievals, and they are the only direct observations of aerosols below, inside and above cloud. Thus, the combination of CAPRICORN, MICRE, MARCUS, and SOCRATES data are synergistic in their characterization of the latitudinal and seasonal variabilities of aerosol–cloud–precipitation–radiation processes over the SO.

Preliminary findings

Much of the initial effort since completing the projects has focused on evaluation of data quality and development of higher-level data products, as well as characterizing cloud and aerosol conditions over the SO. Some of the more noteworthy findings are discussed here. Integration of the datasets and comparison with model simulations and satellite retrievals is starting, a necessary step to evaluate mechanisms responsible for the excess absorption of solar radiation over the SO, which is the overarching objective of these projects.

Latitudinal dependence/composition of surface aerosols. Information on the composition and latitudinal dependence of aerosols is required to understand the origin of aerosols and the role of biological aerosols and sea salt on droplet nucleation in different locations and seasons. Surface aerosol volatility and hygroscopicity were measured during CAPRICORN I at diameters of 40, 100, and 150 nm to provide information about the composition of the Aitken and accumulation modes. Figure 3 shows that the daily averaged number fraction of low volatility aerosol (persisting at 250°C) in the Aitken mode was 0.22 ± 0.2 (mean ± 1σ), which indicates that the Aitken mode was largely composed of secondary non–sea salt sulfates. In the accumulation mode, the mean number fraction of low volatility particles was 0.79 ± 0.2, indicating most particles contained a primary sea spray sourced fraction. Low volatility sea spray particle number fractions, particularly the Aitken mode, increased at higher SO latitudes and were associated with higher wind speeds and generally lower particle number concentrations. The proportion of primary sea spray particles observed from volatility measurements during CAPRICORN I was larger than that observed from BL measurements via scanning transmission electron microscopy (STEM) during SOCRATES in the summer. Further information about aerosol composition and hygroscopicity measurements is provided in the online supplement, which include chemical characterization of single particle composition

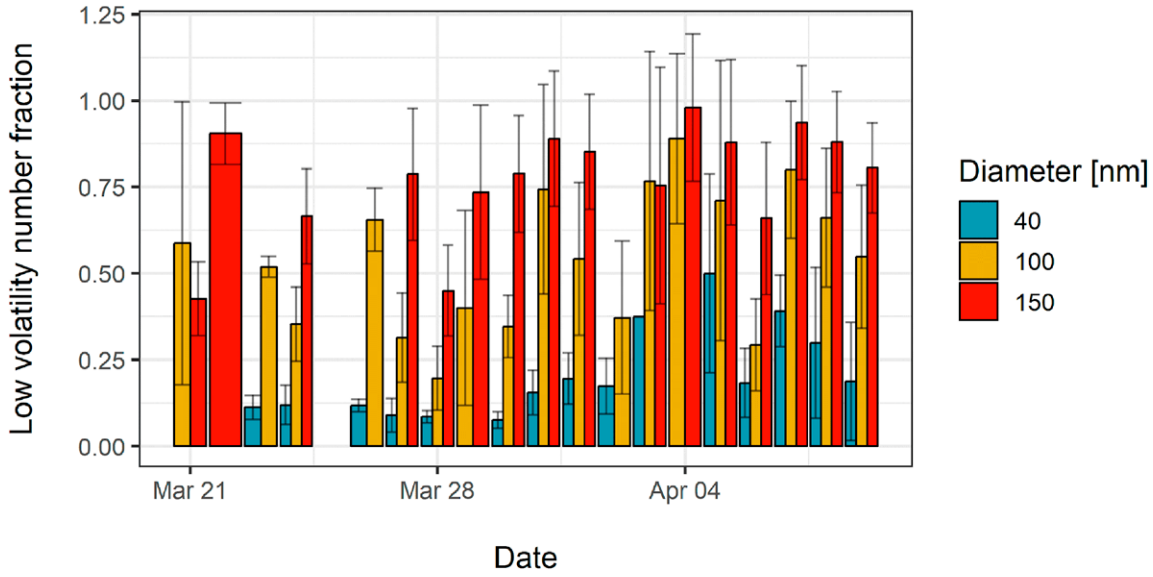

Fig. 3. Daily mean number fraction of low volatility particles measured using the V-TDMA during CAPRICORN I. Preselected particle diameters were 40 nm (blue), 100 nm (yellow), and 150 nm (red). Error bars represent the standard deviation in the daily mean for each preselected particle size.

by scanning transmission X-ray microscopy by near-edge X-ray absorption fine structure (STXM-NEXAFS). These measurements show that particles in-cloud and below-cloud have very similar organic functional group compositions (Fig. ES6).

The average CN number concentrations (diameter greater than 3 nm) during CAPRICORN I were 290 ± 170 cm^{-3}, below typical summertime maxima (Gras and Keywood 2017; McCoy et al. 2015) and hence consistent with the seasonal cycle observed at Cape Grim, with summertime maxima of approximately 500–550 cm^{-3} and wintertime minima of approximately 150 cm^{-3}. The seasonal cycle in SO aerosol number is largely driven by enhanced secondary sulfate production in the summer months (Gras and Keywood 2017; McCoy et al. 2015).

Information on surface fluorescent biological aerosol particles (FBAPs) was provided by the WIBS-4. It measures the fluorescence from single aerosol particles in three excitation/emission channels for particle sizes between 0.8 and 13 μm (Toprak and Schnaiter 2013) to deduce fluorescent (i.e., biological) and total aerosol number concentrations and size distributions. During MARCUS, the FBAP aerosol number concentration was rather low with a median value of 0.43 L^{-1} giving an average FBAP fraction of about 0.3% in the MBL at latitudes from 46° to 68°S consistent with WIBS-4 measurements in other projects. The total number concentration varied strongly with latitude while the FBAP concentration was rather stable with indicated minimum around −56° latitude and increasing concentrations toward the north and south. Implications of these results on the sources and sinks of aerosols over the SO are being examined in several publications under preparation.

BL aerosol and CCN vary according to origin. Aerosol measurements in the BL but above the surface give more information about sources and sinks of aerosols, and their role in droplet nucleation. Ambient aerosols 150 m above the ocean were collected through a CVI inlet on the G-V, but without the counterflow airstream that excludes small particles. Particles in two dry diameter ranges were impacted onto carbon-coated nickel grids or silicon nitride windows and stored frozen for subsequent analysis by analytical STEM and X-ray spectroscopy that produces elemental inorganic composition of individual aerosol particles. The size ranges were about 0.1–0.5- and 0.5–5-μm diameter (50% cut size) for particle densities of 2 g cm^{-3} at 1,000 mb (1 mb = 1 hPa). Based on size distributions from the UHSAS, the 0.1–0.5-μm size

range comprised between 54% and 93% of the aerosol accumulation-mode number concentration (above the Hoppel minimum), and aerosol concentrations > 0.1 μm were similar to nearby cloud droplet concentrations N_c. Thus, particles in this size range would be expected to be representative of the composition of most CCN for the cases analyzed. For the data presented here, heaters on the titanium inlet and stainless steel sample line were turned off to minimize losses of volatile species.

Figure 4 shows STEM results for six flights after grouping particles into different types based on elemental composition and morphology (Twohy and Anderson 2008). Figure 4a shows results for each flight, while Fig. 4b shows the overall mean composition. Particles 0.1–0.5 μm in diameter were dominated by sulfur-based particles (mean 69% by number). Based on the ionic composition measured on the R/V *Investigator* during CAPRICORN II these particles were primarily acidic sulfate, likely with a small contribution from methanesulfonic acid (MSA) and other organics (Twohy et al. 2021). The second-most frequent particle type in this size range (mean 28% by number) was salt-based sea spray. Figure 4b shows different types of sea spray, which were dominated by unprocessed, sodium chloride–based sea spray particles. However, about 40% of sea spray particles were enriched in sulfur and depleted in chlorine through uptake and condensation of sulfur gases (McInnes et al. 1994), and a small percentage (3%) were salts enriched in calcium or magnesium. Crustal and metallic particles and externally mixed organics were also detected in the <0.5-μm population in approximately equal proportions, but were together only about 3% by number. Overall these data indicate that 0.1–0.5-μm particles in the BL were dominated by biogenic sulfates, with a smaller but significant contribution from sea spray. Particles > 0.5 μm (not shown) were dominated by sea spray, with only about 2% other aerosol types. Further, many sea spray particles in the larger size fraction had detectable carbonaceous coatings, which may be important in ice nucleation in the marine environment (McCluskey et al. 2018a).

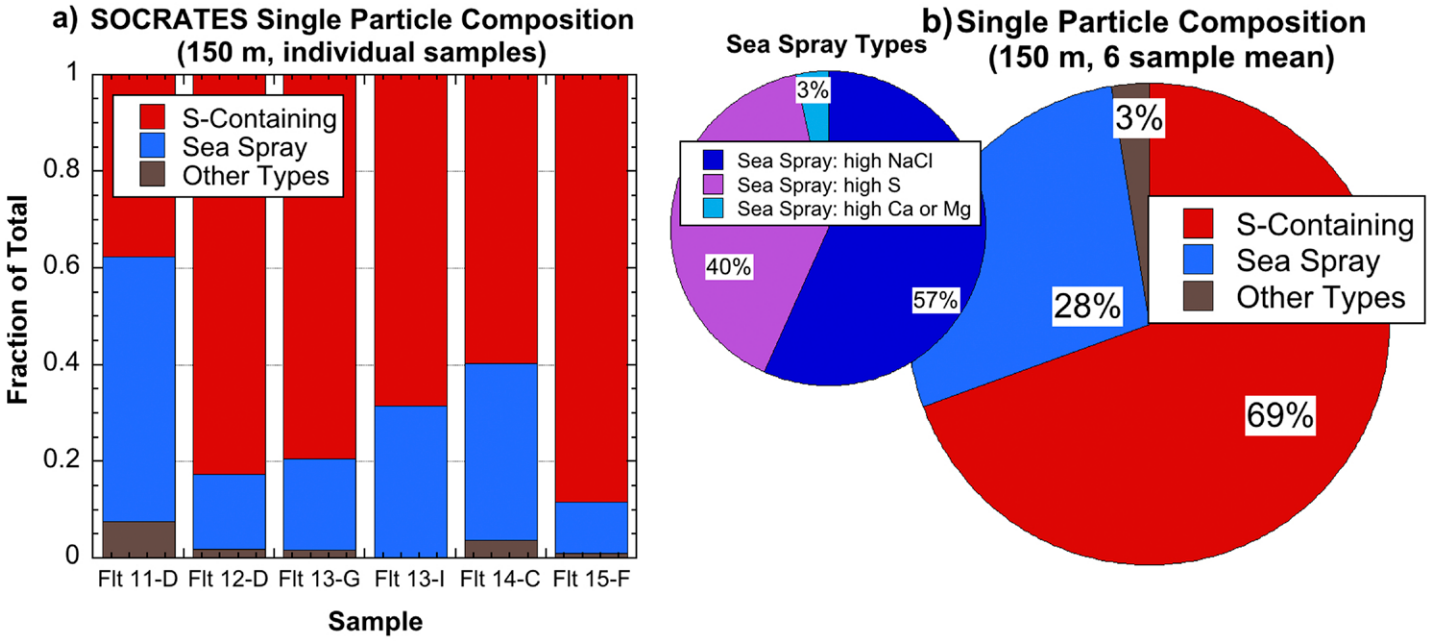

Fig. 4. (a) Compositional fraction of total particles by number in the 0.1–0.5-μm dry size range for six 150-m samples on SOCRATES flights 11–15. (Sample times in UTC: 11-D: 0441:30–0446:30; 12-D: 0453:00–0455:00; 13-G: 0426:20–0431:20; 13-I: 0526:00–0530:00; 14-C: 0422:30–0426:00; 15-F: 0559:40–0604:50.) Categories: S-containing: with S (and sometimes, O) primary elements. Sea spray: Salts of Na, Cl, Mg, S, K, Ca, sometimes with organic coatings. Other types: Includes crustal dust (silicates and carbonates), metals (Al, Fe, Cr, Ti, Mn, Co, Zn, Cu, O, etc.), primary organics (C and sometimes O), and combustion particles (high S, C, O with K). (b) Average composition by number for all six samples; smaller inset further subdivides sea spray into different types of salts.

More information about the chemical composition of the organic compounds is shown in the supplement.

Direct observations of CCN make it possible to understand how aerosols act as CCN. To investigate controls of CCN, the variability in CCN spectra in the BL was characterized using a *k*-means clustering to group into four clusters associated with the observed bimodality in CN and CCN concentrations. Minima in the bimodal frequency distributions of number concentrations occurred at approximately 750 cm^{-3} for CN and was dependent on supersaturation for CCN (Fig. 5a). The four clusters were characterized as follows: 1) low CN/high CCN—southerlies influenced by Antarctic coastal biological productivity; 2) high CN/low CCN—westerlies over the SO characteristic of recent particle formation (RPF) events with low accumulation mode concentrations due to recent precipitation; 3) high CN/high CCN—similar characteristics as high CN/low CCN but with condensational growth of recently formed particles to CCN sizes; 4) low CN/low CCN—aerosol populations scavenged by precipitation and lack of RPF.

The CCN concentrations (at 0.3% supersaturation) correlated well (Fig. 5b) with the overlying N_c indicating large variations in CCN over the SO exist and have an important influence on cloud microphysics. The large variability in CCN led to larger than expected variability in N_c, which ranged from 10 to 449 cm^{-3}. The variation in CN concentration was also notable, ranging from 115 to 1,153 cm^{-3}. To understand this variability, HYSPLIT (Stein et al. 2015; Rolph et al. 2017) back trajectories were performed to identify differences in source location and transport history. The back trajectories for the low CN/high CCN were consistently from the south (Fig. 6d) along the Antarctic coast. This source location is associated with upwelling and marine biological productivity that produces biogenic gases such as DMS, which can oxidize and condense to form CCN-active particles (Hegg et al. 1991; Covert et al. 1992; Andreae et al. 1995; Read et al. 2008; Sanchez et al. 2018). The two clusters with westerly back trajectories (Figs. 6a,b) contained the highest CN. High CN over the pristine SO are likely due to RPF aloft ("New particle formation in free troposphere" section) and mixed downward into the MBL (Sanchez et al. 2018). The high CN/low CCN cluster contained low concentrations of accumulation mode particles (and consequently, small total aerosol surface area) making conditions ideal for particle formation leading to high CN concentrations

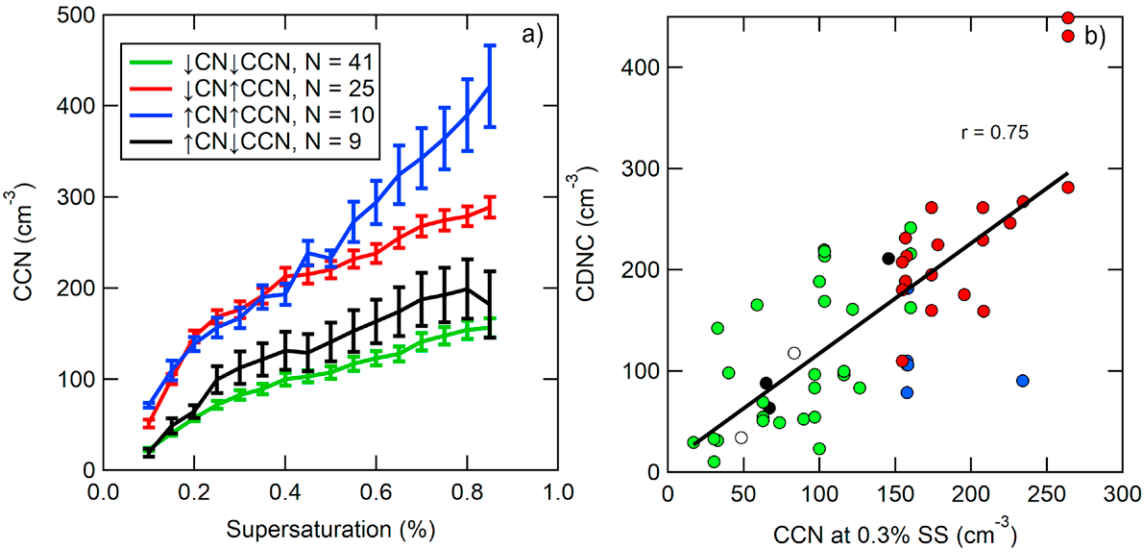

Fig. 5. (a) CCN spectra measured in the marine boundary layer, clustered by CN and CCN concentrations. Error bars represent the standard error. (b) Measured below-cloud CCN concentrations at 0.3% supersaturation vs the observed in-cloud droplet number concentration (CDNC). The black line is a linear fit with *r* = 0.75. The same color scheme used to identify the cluster is used in both figures. The white points in (b) represent measurements that were not clustered due to missing data.

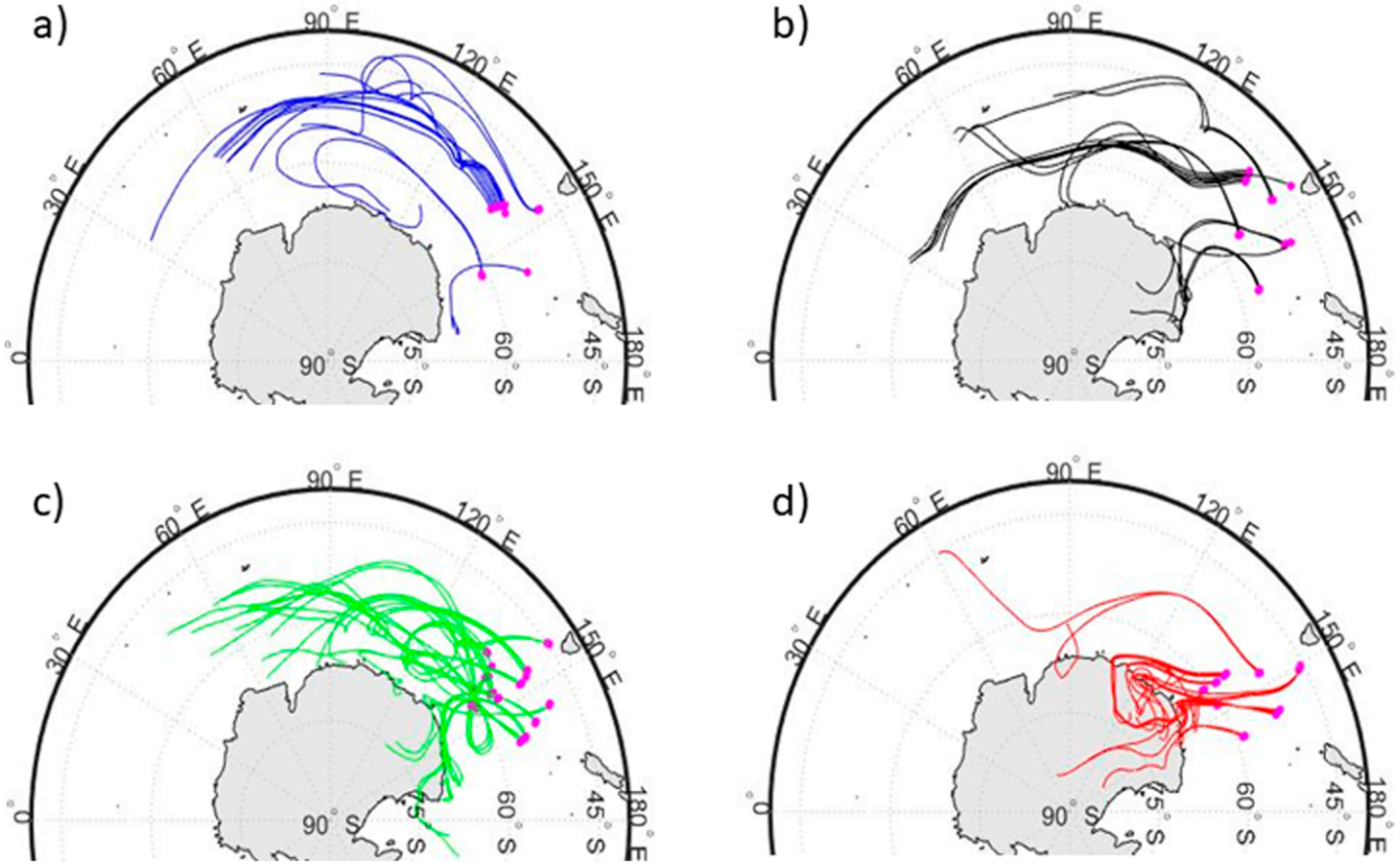

Fig. 6. HYSPLIT 5-day back trajectories for the four clusters shown in Fig. 5, (a) high CN/high CCN, (b) high CN/low CCN, (c) low CN/low CCN, and (d) low CN/high CCN. The magenta circles represent the HIAPER G-V location used to initialize the back trajectory.

(Warren and Seinfeld 1985; Clarke 1993; Pirjola et al. 2000). While the high CN/high CCN cluster did not have low accumulation mode concentrations, the spikes in CCN concentrations at the highest supersaturations (Fig. 5a, >0.6%) are consistent with RPF where some particles grow to CCN sizes, typically through condensational growth during long residence times over the ocean (Russell et al. 1998; Bates et al. 2000; Kulmala et al. 2004; Rinaldi et al. 2010; Zhang et al. 2014). Sanchez et al. (2021) and the online supplement offers more information on how the back trajectories were combined with ECMWF reanalysis to identify relations between BL cloud fraction and particle concentration.

New particle formation in free troposphere. Analysis of free-tropospheric (3–6 km) aerosol measurements from the G-V identified signatures of RPF events occurring frequently across the SO, often in association with synoptic uplift. It is hypothesized that air masses rich in precursor gasses (i.e., emissions from phytoplankton at the surface) undergo rapid synoptic uplift, are processed through the associated convection, cleansed of coarse and accumulation mode aerosol, and released into the free-tropospheric, low-aerosol surface area environment where gas-to-particle conversion is favored (McCoy et al. 2021). This synoptic uplift mechanism is complementary but independent from RPF occurring in the outflow of SO shallow cumulus clouds documented during ACE-1 (Clarke et al. 1998). It is likely both contribute to the widespread observations of high Aitken aerosol number concentrations throughout the SO free troposphere.

A free-tropospheric sample from RF09 is used to illustrate the synoptic-uplift mechanism (Fig. 7). During RPF events, simultaneously low accumulation mode aerosol number

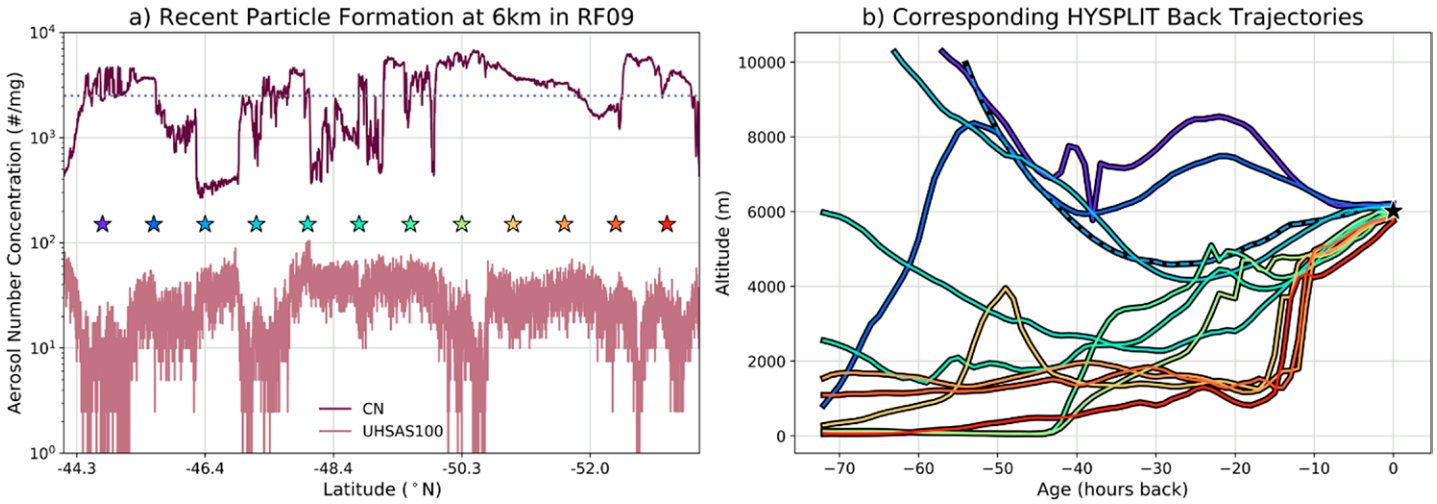

Fig. 7. (a) Time series of total CN (D > 11 nm) and accumulation mode (wing mounted UHSAS, 100 < D < 1,000 nm) aerosol number concentrations sampled in the free tropospheric survey leg (~6 km) of RF09 as the G-V flew south. (b) HYSPLIT 72-h back trajectories of air masses initiated in 10-min intervals [starred locations in (a) with color-coded matched time in (b)] along the G-V flight path. Trajectories dominated by RPF events are identified by where maximum CN over the corresponding 10 min exceeds 2,500 mg^{-1} [dotted line in (a)]. In this case, only one trajectory does not satisfy the criteria for RPF events [dashed line in (b)]. The majority of trajectory ascents exhibit synoptic uplift (3–6 cm s^{-1}) within 20–30 h of SOCRATES sampling (star) and are in proximity to phytoplankton emissions (Z < 1 km) in the prior 72 h.

concentrations (from the wing-mounted UHSAS, 100 < D < 1,000 nm) and high total number concentrations (from the CN counter, D > 11 nm) occur, indicating presence of large Aitken mode concentrations. High concentrations and rapid spatial variability in CN suggest sampling of particle formation bursts or air masses at different stages of nucleation (Clement et al. 2002). RPF occurrences were prolific during RF09 due to a warm conveyor belt occurring west of Australia and propagating south-east toward Antarctica. For statistical airmass evolution analysis, HYSPLIT (Stein et al. 2015) 72-h back trajectories initiated at 10-min intervals along the flight path are identified by maximum CN into RPF (CN_{Max} ≥ 2,500 mg^{-1}) and non-RPF events (CN_{Max} < 2,500 mg^{-1}) (Fig. 7b). Standard temperature and pressure corrected units (mg^{-1}) are used to enable altitude invariant analysis across the campaign. The majority of these RF09 air masses are RPF and have undergone recent synoptic uplift (ascent exceeds characteristic vertical velocity for synoptic events, ~1 cm s^{-1}; Holton and Hakim 2013) in the previous 20–30 h. In the 72-h before sampling, the majority of these air masses have access to the surface (Z < 1 km) and the precursor gases necessary for generating new particles in a low aerosol surface area environment.

RF09 is characteristic of RPF events during SOCRATES and their connection to synoptic uplift. The two most frequent large-scale uplift mechanisms associated with RPF events are warm conveyor belts and subpolar vortices. Volatility analysis via comparison of heated to unheated CN concentrations confirms that the particles sampled during RPF events are likely composed mostly of H_2SO_4, a prominent aerosol precursor gas arising from phytoplankton emissions. It is likely that the high concentrations of Aitken-mode aerosol particles produced above cloud by these RPF events are brought into the BL (Covert et al. 1996) and influence the subcloud CN and CCN concentrations (McCoy et al. 2021; Sanchez et al. 2018) ("BL aerosol and CCN vary according to origin" section). This source of Aitken mode aerosol above cloud may help to buffer SO clouds against precipitation removal, sustaining higher than expected N_c (on the order of 80–100 cm^{-3} between 45° and 62°S), and explains the larger contribution of sulfur-based particles to subcloud CCN compared to sea spray ("BL aerosol and CCN vary according to origin" section; Twohy et al. 2021; McCoy et al. 2021; Sanchez et al. 2021).

Evidence supporting this hypothesis, the broader implications for SO cloud–aerosol interactions, and a more detailed assessment of the synoptic uplift mechanism are presented in McCoy et al. (2021).

Low INP concentrations over SO. To investigate the processes giving rise to extensive SLW over the SO, not only is information about CN and CCN needed, but also about INPs. INP measurements were conducted during the various SO projects to define the spatial and temporal distributions of INPs over the region for the first time since the comprehensive measurements of Bigg (1973). A summary of campaigns, dates and INP sampling methods are given in the online supplement and in Table ES12. Wide regions of the surface marine BL were sampled south of 45°S, while INP measurements on the G-V were tailored to the standard flight patterns.

Figure 8 gives a broad overview of the INP datasets by focusing on the IS data collected during the four ship campaigns. Key findings are the large variability of, but generally very low, INP concentrations at any particular latitude, a weak overall latitudinal dependence, with highest concentrations near landmasses (especially toward Australia), and the large discrepancy with historical measurements over the region, first pointed out in the CAPRICORN I study by McCluskey et al. (2018b). McCluskey et al. (2018b) demonstrated that INP concentrations were up to 100 times lower during CAPRICORN I than measured by Bigg (1973) over some of the same regions, that INPs were (excepting episodic events) often predominately organic in nature with contributions of both heat labile and more stable organics, and that the INP content of Austral summer SO seawater samples were lower than those found in Arctic seawater. These results are consistent with a primary ocean sea spray source of SO BL INPs and also lower derived INP site densities (INPs per aerosol surface area) for immersion freezing in SO air compared to North Atlantic air masses. Using CAM5 with constrained meteorology, McCluskey et al. (2019) demonstrated that using parameterizations linking the number concentrations of mineral dust and surface area of sea spray aerosols in the global aerosol model could predict the magnitude of INPs observed in CAPRICORN I, and that sea spray organic INPs dominated on average, but that episodic incursions of inorganic mineral dust INPs present in the middle troposphere could occur and then dominate ice nucleation in the MBL. This vertical structure of compositions is demonstrated in analyses of collected aerosol compositions above, below and within clouds during SOCRATES (Twohy et al. 2021).

The INP datasets remain to be fully explored to investigate spatial, temporal and compositional variabilities, through aligning with aerosol data including real-time bioaerosol and next-generation DNA sequencing of bacteria. Those bacterial sequencing analyses have been completed for aerosol samples collected on equivalent filters to the INP units during CAPRICORN II. Results reported in Uetake et al. (2020) indicate the predominance of marine bacteria in the

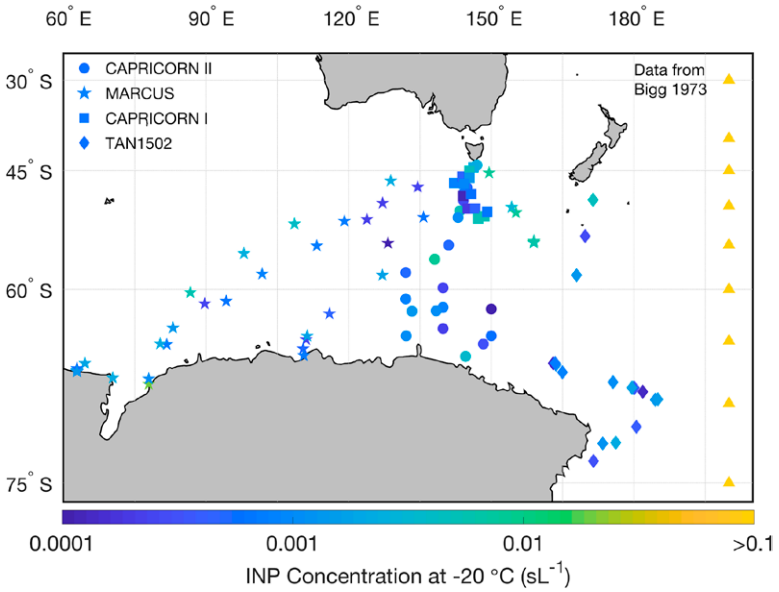

Fig. 8. INP number concentrations per volume of air at –20°C over the SO region for a selection of the studies (MARCUS, CAPRICORN I, CAPRICORN II, TAN1502) listed in Table ES12. Each data point represents the midpoint position of a single filter collection. Historical data from Bigg (1973) are shown at right for context (each is the mean of numerous measures at that latitude); all are the same color since all were >0.1 per standard liter (sL^{-1}).

MBL during the ship campaign, confirming the pristine marine source of aerosols, and thus INPs, under most circumstances in this region. Comprehensive INP data from all SO studies will ultimately be normalized for use in parameterization development (see, e.g., McCluskey et al. 2018c, 2019; Vignon et al. 2021), and will serve as a basis for constraining primary ice nucleation for comparison with observations of ice formation and numerical model simulations of SO clouds.

Clouds: In situ observations of variability in liquid cloud droplet number concentration. In situ G-V observations allow for process studies to investigate aerosol–cloud interactions and processes controlling distributions of SLW. For example, using data obtained during four ramped ascents and descents through BL clouds, Fig. 9 shows N_c measured by the CDP as a function of altitude. Although all profiles were collected in a similar geographical area on two different days, there is considerable variability in N_c, ranging from less than 50 cm^{-3} near cloud top on RF08 at latitude 55.8°S to greater than 450 cm^{-3} near the top and in midcloud layer for the same flight further south at 58.7°S. Although some lower N_c, such as concentrations of about 50 cm^{-3} seen on RF04, were associated with lower wind speeds averaging 5.5 m s^{-1}, and some higher concentrations of 250 cm^{-3} on RF08 at 59.9°S and up to 450 cm^{-3} on RF08 at 58.7°S were associated with larger wind speeds averaging 20.5 and 22.0 m s^{-1}, respectively, correlation with wind speed was not always the case (e.g., low N_c of less than 50 cm^{-3} on RF08 at 55.8°S occurred when wind speeds were 26.6 m s^{-1}) as updrafts, dynamics, turbulence, and coupling of the cloud with the surface layer can also affect N_c. Thus, while generation of sea salt CCN caused by breaking waves associated with high winds likely contribute to variations in N_c, other factors also contribute significantly, such as the influence of source regions with different bioactivity on the production of CCN and the degree of coupling between the surface and cloud.

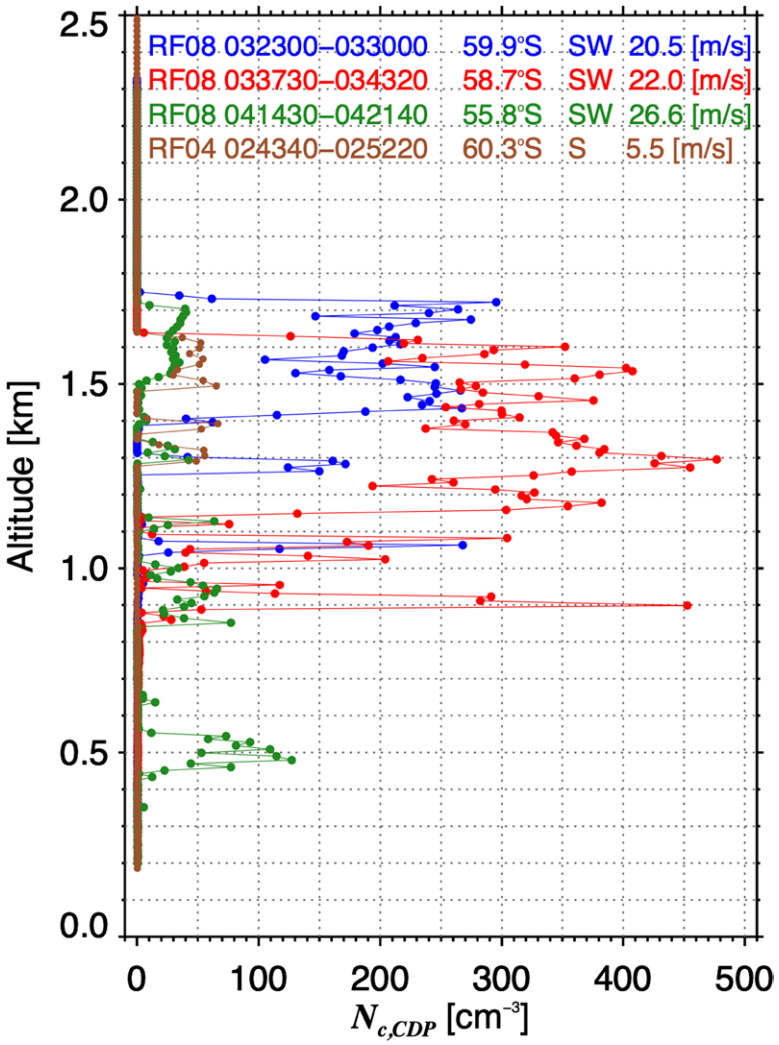

Fig. 9. Cloud droplet concentration measured as a function of altitude for four ramped ascents/descents through boundary layer cloud for the days indicated in the legend. The time period, average latitude, and average wind speed of each ascent or descent are indicated. Each circle represents a 2-s average.

Variable but prevalent supercooled water observed in situ. Although SLW dominated many BL clouds observed during SOCRATES, information about ice crystals, when present, is important for understanding SLW persistence and cloud glaciation. During SOCRATES ice particle number concentrations and high-resolution images were acquired over a large range of temperature with optical array probes and the PHIPS probe. Using cloud phase determined with a combination of in situ cloud probes (J. D'Alessandro et al. 2021, manuscript submitted to *J. Geophys.*

Res. Atmos.), Fig. 10 shows the distributions of phases as a function of temperature. In some instances, even the identification of phase is poorly defined (e.g., Korolev et al. 2017) as, for example, there is no consensus on how many ice crystals need to be mixed within a sample volume of water drops to be mixed- rather than a liquid-phase cloud. For analysis of in situ data, the term mixed-phase refers to the occurrence of a liquid mass fraction between 0.1 and 0.9 in a 1-s time period as calculated using data from a combination of size-resolved and bulk mass in situ probes. In addition to the frequent presence of clouds made exclusively of SLW at very low temperatures, another notable feature was the frequent observation of glaciated clouds at relatively high temperature corresponding to the Hallett–Mossop (H-M) range of $-2°C < T < -8°C$. Figure 11 shows a collection of representative ice particles images captured by the PHIPS during RF02 between 0° and −5°C. Typical ice particle habits were needles that were frequently rimed, thus acting as possible rime splintering sources in the H-M process. Smaller ($D < 100$ mm) pristine hexagonal columns and plates were also observed that possibly grew from ice splinters (Korolev et al. 2020) (Fig. 11, first row). Some of the pristine small particles were observed to have been scavenged by the larger needles and needle aggregates (Fig. 11 third row, second needle from the left). Occasionally, frozen drizzle droplets were detected—either as complete or sometimes as fractured particles (Fig. 11, second row).

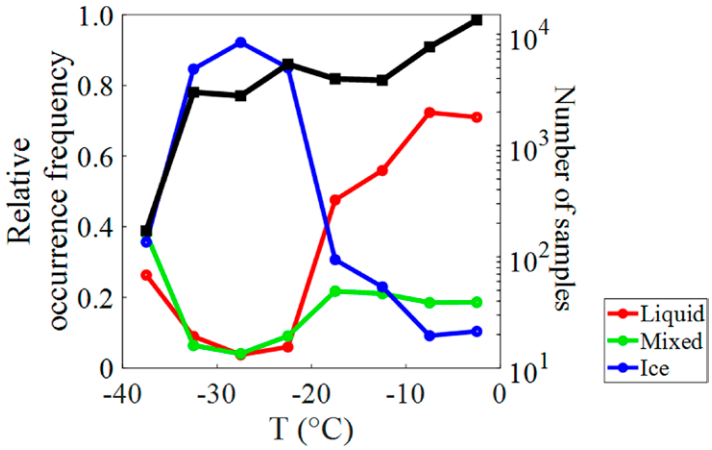

Fig. 10. Relative occurrence frequency of different phases derived from suite of in situ probes as a function of temperature (adapted from J. D'Alessandro et al. 2021, manuscript submitted to *J. Geophys. Res. Atmos.*). The black line indicates the number of samples, giving some information about statistical significance of results.

The presence of small horizontal scale generating cells were noted near the tops of BL stratocumulus and higher cloud layers in the free troposphere. Such cells are small regions of high reflectivity that frequently produce precipitation streaks below. Although such cells have been observed in other environments, such as the Arctic (McFarquhar et al. 2011) and midlatitudes (Plummer et al. 2014), the cells observed over the SO had smaller horizontal scales and thus their structure and properties need to be determined to understand precipitation development and cloud life cycles. Wang et al. (2020) provide this characterization using times when the G-V was flying near cloud top. Figure 12 shows an example of their approach whereby the probability distribution functions of liquid water content, total concentration, and ice water content were compared inside and outside of generating cells identified by the HCR. All three parameters are higher to a statistically significant degree inside the cells, but substantial liquid water and numbers of particles also occur outside the cells. This shows that although the cells provide a favorable environment for particle nucleation and growth, turbulent mixing at cloud top reduces the gradients inside and outside of the cells. The online supplement gives extra information on how the combination of in situ and remote sensing measurements can be used to identify and characterize the finescale structure of SLW, SLD, drizzle, and ice crystal type.

Fig. 11. Collection of PHIPS images of ice particles from RF02 sampled in the temperature range from 0° to −5°C.

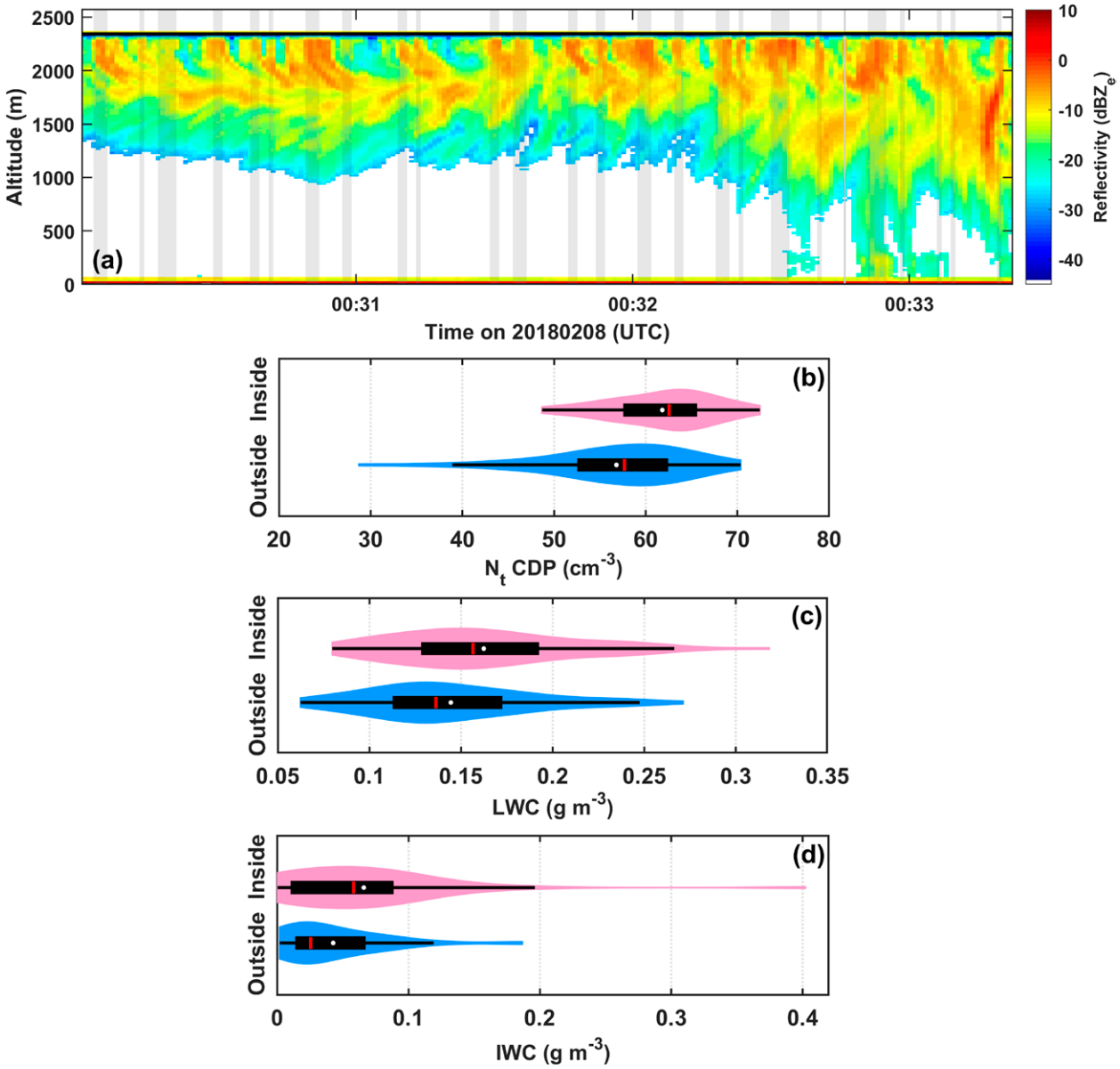

Fig. 12. (a) Altitude–time cross section of HCR equivalent reflectivity factor Z_e over the time period between 0030 and 0034 UTC 8 Feb 2018. The black line shows the flight level of the G-V aircraft, and the shadows represent the location of the generating cells identified by the method of Wang et al. (2020). Other plots show statistical analysis of data collected over this time as shown by kernel probability distribution functions of properties inside (pink) and outside (blue) of generating cells for (b) N_t, (c) LWC, and (d) IWC. Black boxplots show 5th, 25th, 50th (red line), 75th, and 95th percentiles of data. White points indicate the mean value. The width of the red and blue shaded area represents the portion of data located at particular value.

The location of liquid water is of interest not only for understanding cloud microphysical process and radiative properties, but also for assessing the potential hazard posed by aircraft icing when the liquid is supercooled. Icing is a significant hazard for aviation, especially over the SO, and is most concerning as the droplets become large enough to impact on areas not typically protected by anti-icing or de-icing systems. Small cloud droplets ($D < 50$ μm) tend to impact on forward edges of aircraft as seen in Fig. 13, while larger drops tend not to freeze on impact and instead flow back farther before freezing or else are heavy enough to be somewhat independent of the airflow and actually impact the aircraft behind the forward edges (Fig. 13b) (FAA 2015; Cober and Isaac 2012). Known as supercooled large drops (SLD), they can accrete on the wing and other important control areas of the aircraft which are outside

the heated surfaces. Freezing drizzle and freezing rain are examples of SLD.

Observing secondary ice production (rime splintering) over SO. Two research flights (RF11 and RF15) during SOCRATES were dedicated to the sampling of shallow cumulus clouds in the cold sector of extratropical cyclones to understand the possible maintenance of SLW in those clouds. Mossop (1970) had found ample evidence of secondary ice production by rime splintering in cumuli sampled off the western and eastern coasts of Tasmania. Because of the need to focus sampling at multiple levels in the same cumulus field, there was insufficient time to sample the cumuli using the standard curtain flight pattern to 60°S. Thus a population of cells as far south as possible, near 55°S, was identified for sampling. Thereafter the G-V flew a series of constant altitude legs about 15 min long targeting the tops of actively growing cells, and also sampling at and below cloud bases, and above the cloud tops, to measure aerosol, CCN and INPs. These two SOCRATES flights provided clear evidence of rime splintering, farther away from land sources than documented before. Of the 34 sampled shallow cumuli occupying temperatures where rime splintering can act (from –3° to –9°C), 47% contained regions where ice crystals were orders of magnitude more than the INP observed (Scott 2019). The SOCRATES airborne radar data captured the cloud macrostructure needed to place the in situ microphysical data collected near the cloud tops in context (Fig. 14). A complex, multithermal structure was common in clouds exhibiting the features of rime splintering, and lacking in clouds that only contained SLW. These new data are being used to guide and constrain detailed process-level numerical modeling, to understand why some SO cumuli glaciate by this mechanism, while others do not.

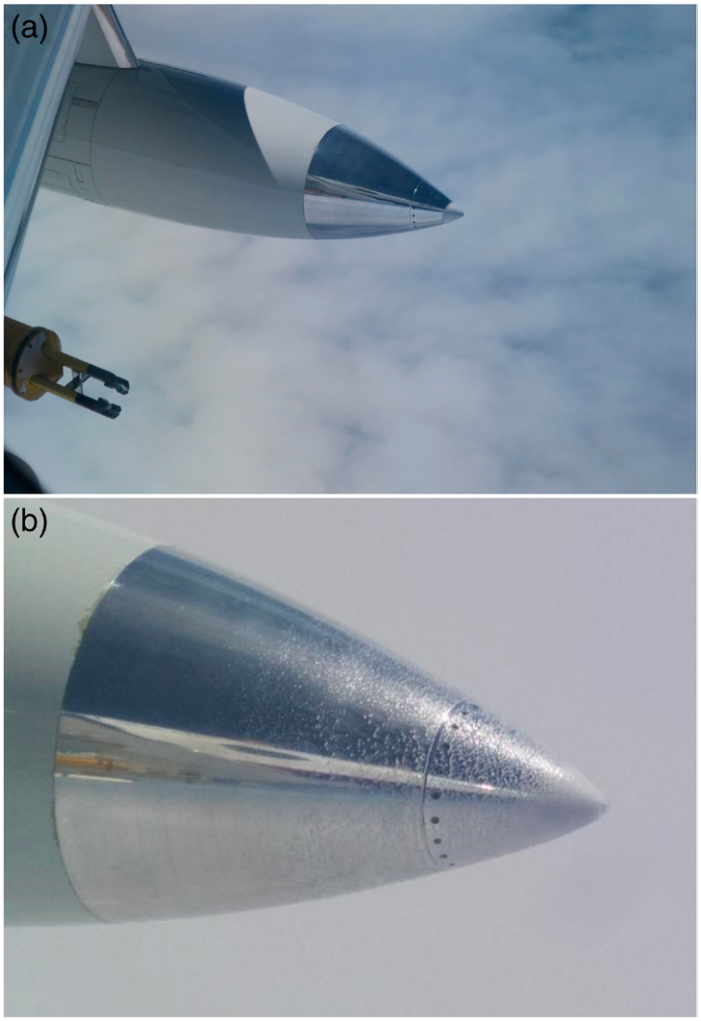

Fig. 13. (a) The nose cone of the NSF–NCAR G-V aircraft large wing pod during an encounter with small supercooled cloud droplets during SOCRATES. Ice has accreted on the tip of the pod. (b) The nose cone of the G-V wing pod under conditions where larger supercooled droplets were encountered. Notice the drops have impacted and run back before freezing further back on the pod.

Himawari-8 *retrievals consistent with field observations.* Satellite data provide both a large-scale context for interpretation of finer-resolution remote sensing data and in situ measurements. The *Himawari-8* satellite, developed and operated by the Japan Meteorological Agency, has provided a significant advance in geostationary satellite capability over the Asia–Oceania region. It provided rapid updates on meteorological conditions and cloud systems throughout the SO campaigns which were especially critical for aircraft operations.

Figure 15 shows the frequency of occurrence of *Himawari-8* cloud type (Pavolonis 2010) as a function of cloud-top temperature (Heidinger 2011) for the 15 SOCRATES flights. For the duration of each flight, data are taken from a rectangular area that extends from 45°

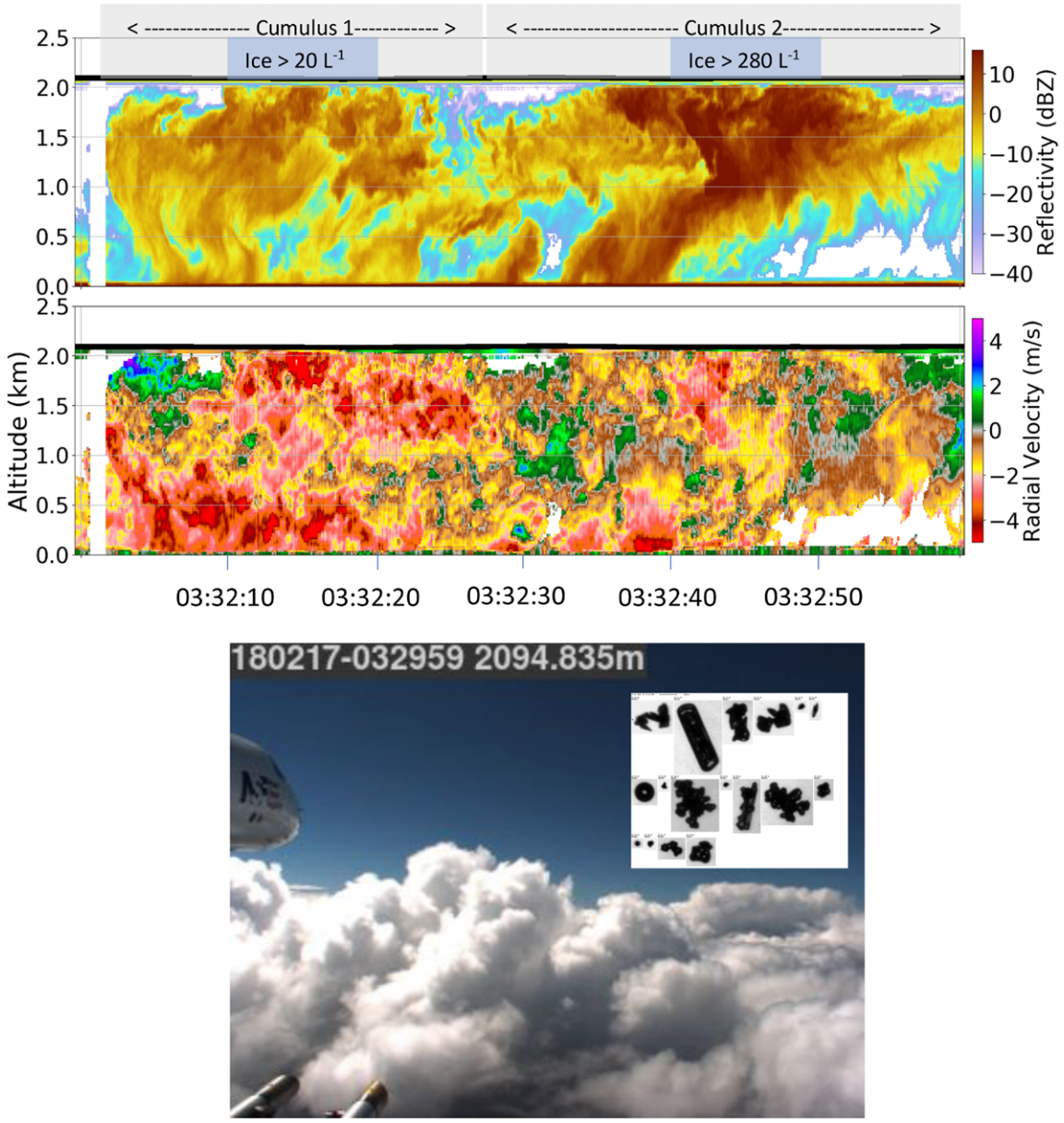

Fig. 14. Aircraft pass on 17 Feb 2018, through the tops of two closely spaced cumuli at a temperature of –9°C, as shown by the downward-pointing airborne Doppler radar on the G-V aircraft [(top) radar reflectivity and (middle) vertical velocity; positive values denote upward motion of particles]. The black horizontal line at the top shows the aircraft location as it passed through the cloud tops. Shaded gray boxes demarcate the two clouds, with shaded blue boxes identifying 10-s regions with the highest maximum ice number concentrations (corrected for possible shattering artifacts) as labeled. (bottom) Snapshot from forward video also shows the multiple thermal structure of these cumuli as the aircraft approached. (inset) Particle images from PHIPS probe indicated rimed ice and liquid drops were present, necessary for rime splintering to be active, as well as the expected products of rime splintering, pristine, and rimed columns.

to 63°S and covers the entire width of the flight track. The statistics represent the overall atmospheric and cloud conditions sampled during both the in situ and remote sensing sampling legs. Figure 15 highlights the prevalence of SLW cloud tops for 0°C > T > –25°C. More details of this *Himawari-8* cloud classification can be found in Huang et al. (2019), and information about how the in situ cloud properties are being used to evaluate cloud microphysical properties is included in the online supplement.

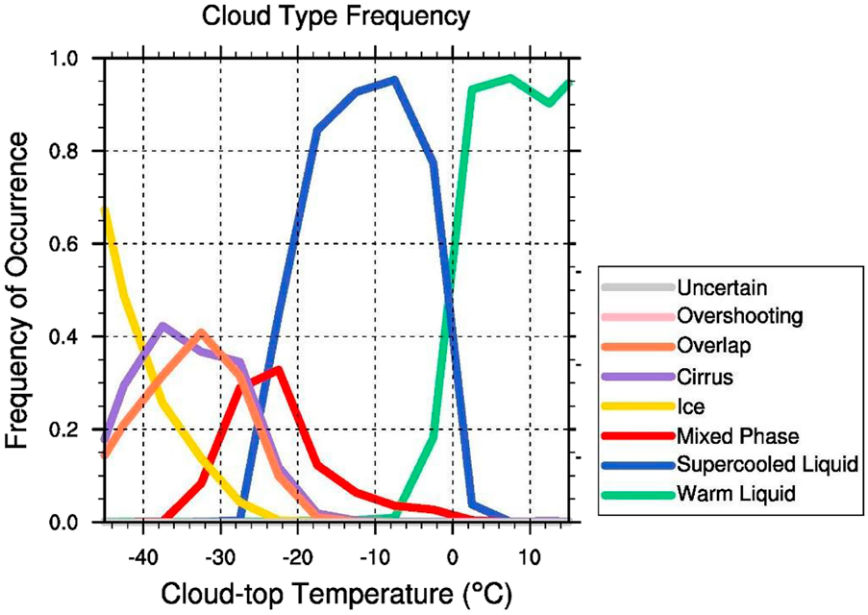

Fig. 15. Frequency of occurrence of Himawari-8 cloud type as a function of cloud-top temperature for the 15 SOCRATES missions (includes times for both outbound and inbound legs).

Radiative fluxes confirm bias in climate models. Many studies involving surface radiative fluxes rely on fluxes retrieved from satellites, primarily from the Clouds and the Earth's Radiant Energy System (CERES) instruments or derived from spaceborne cloud radar and lidar observations (*CloudSat–CALIPSO*). Based on CERES data, most climate models participating in CMIP5 had excessive SW radiation reaching the surface over the SO (Zhang et al. 2016). An evaluation of CERES Synoptic (SYN) and Energy Balanced and Filled (EBAF) edition 4 and *CloudSat* retrieved surface SW and longwave (LW) downwelling fluxes against surface observations collected during MICRE (Hinkelman and Marchand 2020) finds that the overall biases in the CERES-surface fluxes are modest, but slightly larger at Macquarie Island than at most other locations, approximately +10 W m^{-2} for the SW and –10 W m^{-2} for the LW in the annual mean. The SW bias is positive meaning that climate model biases in downwelling SW fluxes are, if anything, slightly larger than previous studies suggest because CERES downwelling fluxes may be a bit too large and model fluxes are larger yet. However, both the SW and LW bias have significant seasonal and diurnal variations, with SW biases being near +20 W m^{-2} during the SH summer. Biases in LW fluxes are much larger at night (–16 W m^{-2}) than during the day (<2 W m^{-2}) with significant seasonal variations controlled by the relative ratio of daytime versus nighttime, and consequently are largest during the SH winter. This thus confirms that the climate model biases that motivated the projects are indeed real.

Low clouds responsible for much of climate model bias. Understanding the contributions of different cloud types to the surface SW radiation bias in models is a major objective of these field campaigns, which complements the analysis of large-scale environments most conducive to such biases. Figure 16 shows the observed and modeled surface cloud radiative effect (CRE) during CAPRICORN I for different cloud cover types using the BoM ACCESS-C3 numerical weather prediction system (4-km horizontal resolution, no data assimilation, downscaled from the regional 12-km-resolution model), which was run for the campaign period. The observed CRE is the difference between the measured downwelling radiative flux at the surface and the simulated clear-sky downwelling radiative flux, accounting for ocean albedo and the broadband infrared emissivity of seawater (e.g., Protat et al. 2017). Over the CAPRICORN I period, the mean SW CRE was –66.7 W m^{-2}, partially offset by a mean LW CRE of 44.4 W m^{-2}, resulting in a mean net CRE of –22.3 W m^{-2} (Fig. 16d). A 1-min merged cloud radar–lidar product from ship-based measurements was used to classify the observed cloud profiles into different cloud cover types (Noh et al. 2019) at 1-h resolution to compare with model outputs. Hours that contained only clear skies were classified as clear. Hours that contained more than 30 min of clear skies were classified as "mostly clear." Because the cloud

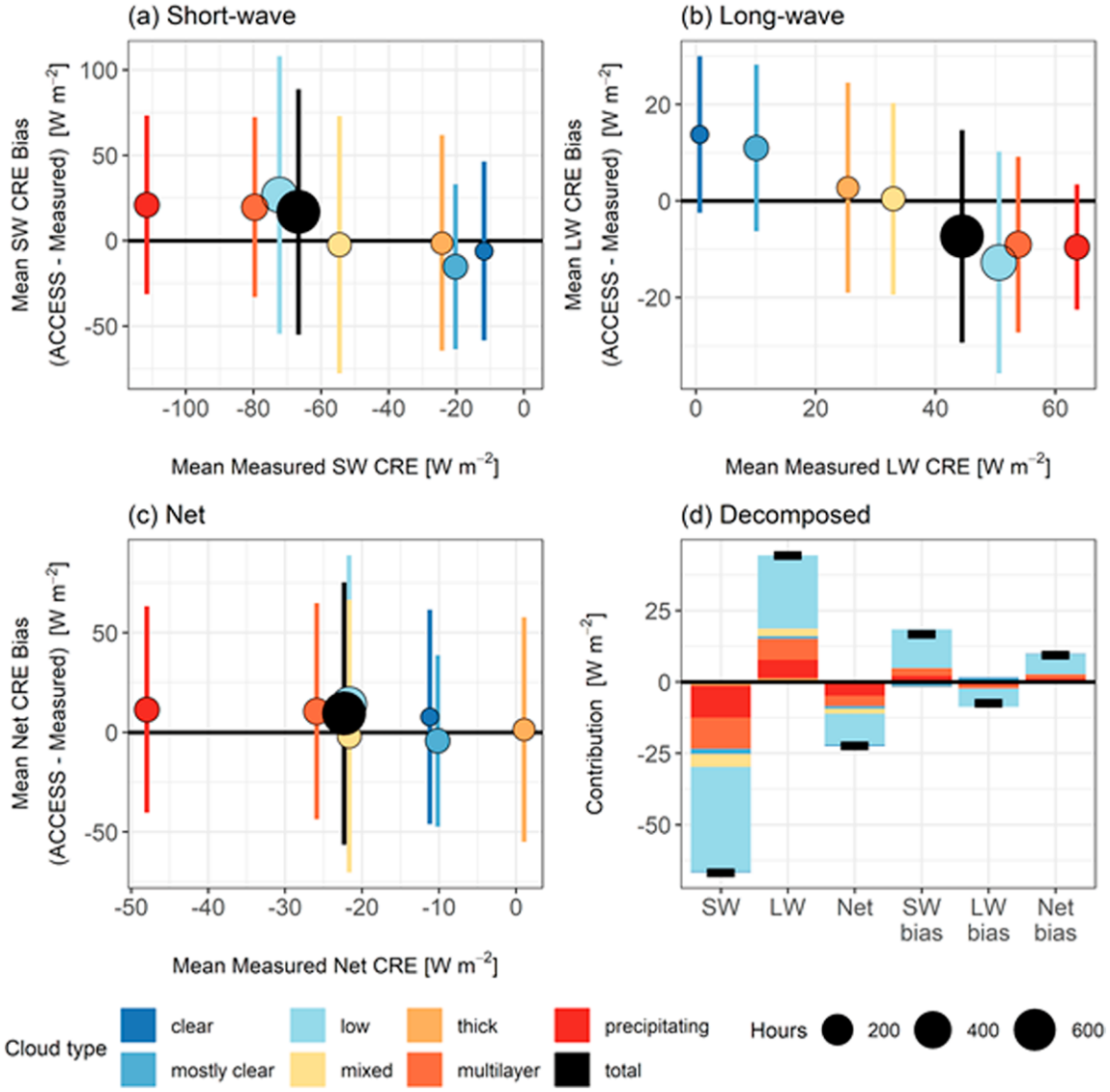

Fig. 16. The mean CRE biases [(a) shortwave, (b) longwave, and (c) net] in ACCESS-C3 relative to the mean measured CRE for different cloud types over the Southern Ocean during CAPRICORN I. Vertical error bars represent the standard deviation of each CRE bias for each cloud type. The size of the points is proportional to the number of sampling hours of each cloud type. (d) The decomposed CRE and CRE biases, weighted by the relative frequency of occurrence for each cloud type. The black horizontal bars represent the total CRE and CRE biases for the whole campaign.

cover types containing clouds overlapping low-, mid-, and high-altitude slabs made up only 5% of all the observations, they were grouped into a "thick" cloud type classification. Hours that contained at least 15 min of precipitating clouds were classified as precipitating, even if one of the other conditions was met. Last, hours that did not meet any of these conditions were classified as "mixed."

During CAPRICORN I, 51% of the 697 observation hours were characterized by low clouds, followed by multilayer (14%), precipitating (10%), mostly clear (10%), mixed (8%), thick (5%), and clear conditions (2%). Large negative SW CREs are observed for precipitating, multilayer and low cloud categories and these correspond to a mean positive SW CRE bias for all three clouds types, meaning too much SW flux is reaching the surface in the model under these conditions (Fig. 16a). The negative SW CRE and positive SW CRE bias was partially offset by positive LW CREs and a negative LW CRE bias for these cloud types (Fig. 16b). This resulted in a net negative CRE and a positive net CRE bias for precipitating, multilayer and low clouds (Fig. 16c). While smaller negative (positive) SW (LW) CREs were observed for

the other cloud types, the CRE biases for these had little impact on the overall CRE and CRE bias once weighted by their respective frequency of occurrence (Fig. 16d). For the measured SW, LW, and net CRE, low clouds were responsible for just over half of the total contribution during CAPRICORN I, with most of the remaining contributions from multilayer and precipitating clouds. Interestingly, however, low clouds were responsible for nearly all of SW, LW, and net CRE biases in ACCESS, highlighting again the need to focus our attention on better understanding these low clouds. This work is being extended to include the MARCUS, MICRE, and SOCRATES observations.

Remote sensing data also show prevalence of supercooled water. The online supplement summarizes studies that have used the CAPRICORN and MARCUS data to determine the frequency of and sources of SLW over the SO. To further understand processes responsible for the production and maintenance of SLW over the SO, and to understand the seasonal and latitudinal dependence of cloud properties, the MARCUS cloud retrievals were combined with a value added product developed to describe the environmental quantities at the position of the *AA* at 10-min resolution. Parameters examined include ship navigation parameters, local meteorological conditions, SST, location of the *AA* relative to the oceanic polar front, lower tropospheric stability, marine cold air outbreak index, inversion height, lifting condensation level, location relative to the center of the nearest cyclone, warm front and cold front and location of air parcels 72 h prior to their arrival at the ship computed from HYSPLIT. Consistent with prior satellite retrievals, the MARCUS data show that low-level liquid water clouds are ubiquitous over the SO and that much of the water is supercooled. For instance, south of 60°S over 49% of nonprecipitating clouds had cloud base $T < 0$°C and mean liquid water paths greater than 50 g m^{-2} as measured by the microwave radiometer. Figure 17 shows an example of the analysis illustrating how the properties of single-layer, nonprecipitating clouds with bases less than 3 km and greater than 500 km away from the nearest cyclone center varied depending on whether the measurements were made north or south of 60°S. The retrievals show that with average cloud base T of about −10°C south of 60°S and hence the location of the

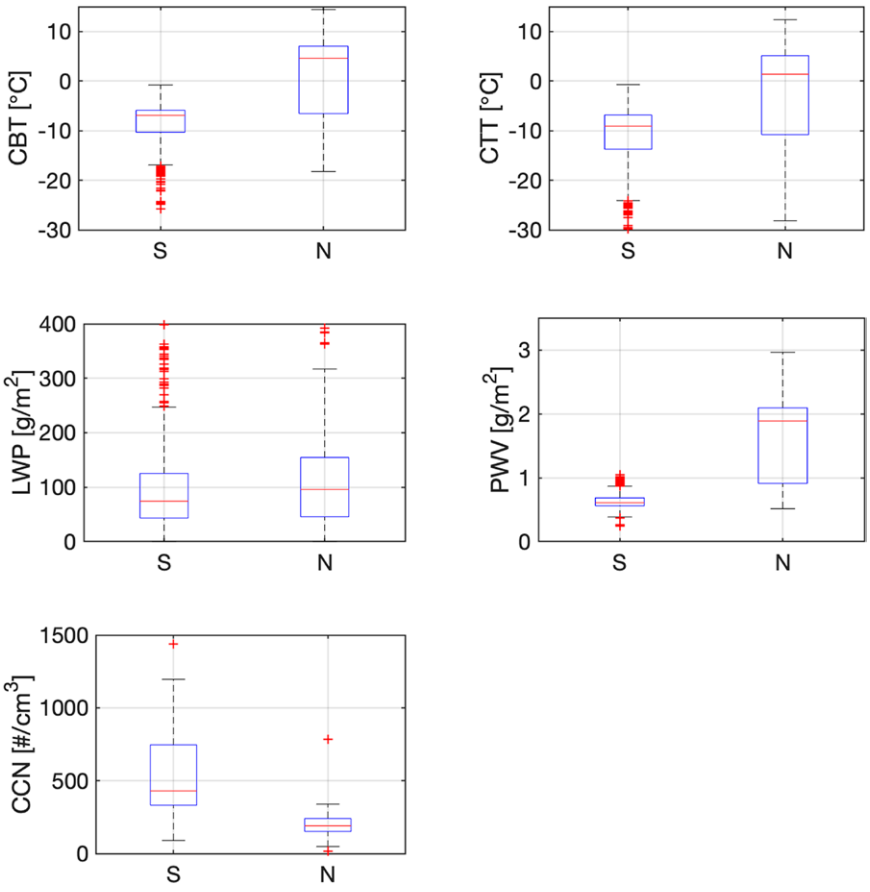

Fig. 17. Statistical distribution from MARCUS cruises of how cloud and environmental properties varied depending upon whether measurements were north or south of 60°S for time periods with single-layer, nonprecipitating clouds with bases less than 3 km and greater than 500 km away from nearest cyclone center. Box-and-whisker plots show quartiles of the distribution, the red line indicates mode, black bars are defined as $q_3 + 1.5 \times (q_3 - q_1)$ and $q_1 - 1.5 \times (q_3 - q_1)$, where q_1 and q_3 are the 25% and 75% percentiles, and red pluses all points outside the black bars.

oceanic polar front, SLW must extensively exist even though there is less precipitable water than north of 60°S. Further, CCN concentrations and retrieved N_c peaked in December, but there were large variations over all seasons. Similar ongoing analysis is quantifying the dependence of cloud properties on environmental and aerosol conditions, from which processes responsible for SLW can be better elucidated.

Precipitation observations. Recent evaluation studies of satellite rainfall products have highlighted large statistical discrepancies (up to a factor 2) in zonal precipitation averages derived from GPM, *CloudSat*, and the Global Precipitation Climatology Project (GPCP) south of 40°S and north of 40°N (Grecu et al. 2016; Skofronick-Jackson et al. 2017). Shipborne disdrometer and active remote sensing observations collected during CAPRICORN have been used along with others from several research vessels as part of the Ocean Rainfall And Ice-Phase Precipitation Measurement Network (OceanRAIN) project (Klepp et al. 2018) to establish whether these differences between satellite rainfall products are driven by latitudinal differences in statistical properties of the drop size distribution (DSD) and associated assumptions in GPM radar rainfall retrievals. Results from these investigations are summarized in Protat et al. (2019a,b). A large natural, latitudinal, and convective-stratiform variability of the DSD was clearly found, with a much lower drop concentration for diameters smaller than 3 mm and a very different modal value of the DSD shape parameter distribution (μ) to that assumed in the GPM algorithms in the SH high latitude (south of 45°S) and NH polar latitude (north of 67.5°S) bands (Protat et al. 2019a). From a radar rainfall retrieval perspective, the attenuation–reflectivity, drop diameter–reflectivity, and rainfall rate–reflectivity relationships in the SH high latitude and NH polar latitude bands are found to be fundamentally different from those at other latitude bands, producing smaller attenuation, much larger drop diameters, and lower rainfall rates for a given reflectivity, which potentially explains the observed discrepancies between satellite rainfall products (Protat et al. 2019b). Evaluations of *CloudSat* and other satellite precipitation datasets using MICRE and SOCRATES datasets are underway, and will be reported in future publications.

Unique view of BL structure from soundings. Across the four field campaigns, a total of 2,186 soundings were obtained. While a variety of spatial and temporal biases exist in the sampling, the collection provides an unprecedented view of the thermodynamic structure of the lower troposphere across the SO. A simple *k*-means cluster analysis on the lower thermodynamic variables [*T*, relative humidity, winds (u and v) at 700-, 850-, and 925-hPa levels, and surface pressure, *T*, and relative humidity) (Lang et al. 2018) produces a cluster along the Antarctic coast (C2), another at high latitudes (C1, 55°–65°S), where polar mesovortices are commonly present, and multiple clusters at lower latitudes across the SO storm track (40°–60°S). Increasing the numbers of clusters effectively isolates different sectors of the midlatitude storm track. For brevity the storm track clusters are merged into a single cluster (M).

The composite soundings for M, C1, and C2 (Figs. 18a–c) illustrate differences in the thermodynamic structure of the atmosphere across the SO. The M composite features strong westerly winds and a low-level inversion near 900 hPa. BL clouds are commonly observed across this region. C1 covers the region where the greatest bias exists in the regional energy budget (Trenberth and Fasullo 2010) and it is also the region where multilayer clouds are commonly detected by A-Train satellites (Mace et al. 2009). For the C1 composite (Fig. 18b), the low-level winds are very weak and the atmosphere is near saturation at all altitudes. A more complete analysis of individual soundings (not shown) confirms that multilayer clouds are frequent, but relatively few inversions are present, which suggests that the polar mesovortices mix the lower free troposphere and that the weak winds may allow for a radiative equilibrium to weaken inversions. Finally, along the Antarctic coast (C2), the composite reveals a very dry,

cold atmosphere, commonly cloud free. An illustrative back trajectory (Fig. 18d) illustrates that the low-altitude dynamics may be dominated by strong Antarctic outflows such as katabatic winds draining cold, dry air off the Antarctic plateau onto the SO. Using a cyclone tracking algorithm (Lim and Simmonds 2007) on the ERA5 reanalysis, we plot the location of the soundings, by cluster, to the nearest cyclonic core (Fig. 18e). The M soundings typically reside to the north of core, the C1 soundings commonly reside just poleward of the core, while the C2 soundings reside, on average, about 5°S of polar mesovortices (Truong et al. 2020).

Impact of biological particles on CCN/droplet concentrations near Antarctica. The online supplement summarizes the use of remote sensing data to derive cloud microphysical properties (Mace and Protat 2018; Mace et al. 2020). In Fig. 19, a time series of daily mean N_c retrieved from nonprecipitating liquid MBL clouds during CAPRICORN II is shown. The N_c represents the mean value from an entire 24-h period with the error bars showing the standard deviation of the total number of successful retrievals for that day where each retrieval is valid for a 30-s interval (Fig. 19e). The latitude of the ship during the 24-h period is shown in Fig. 19d. Cloud

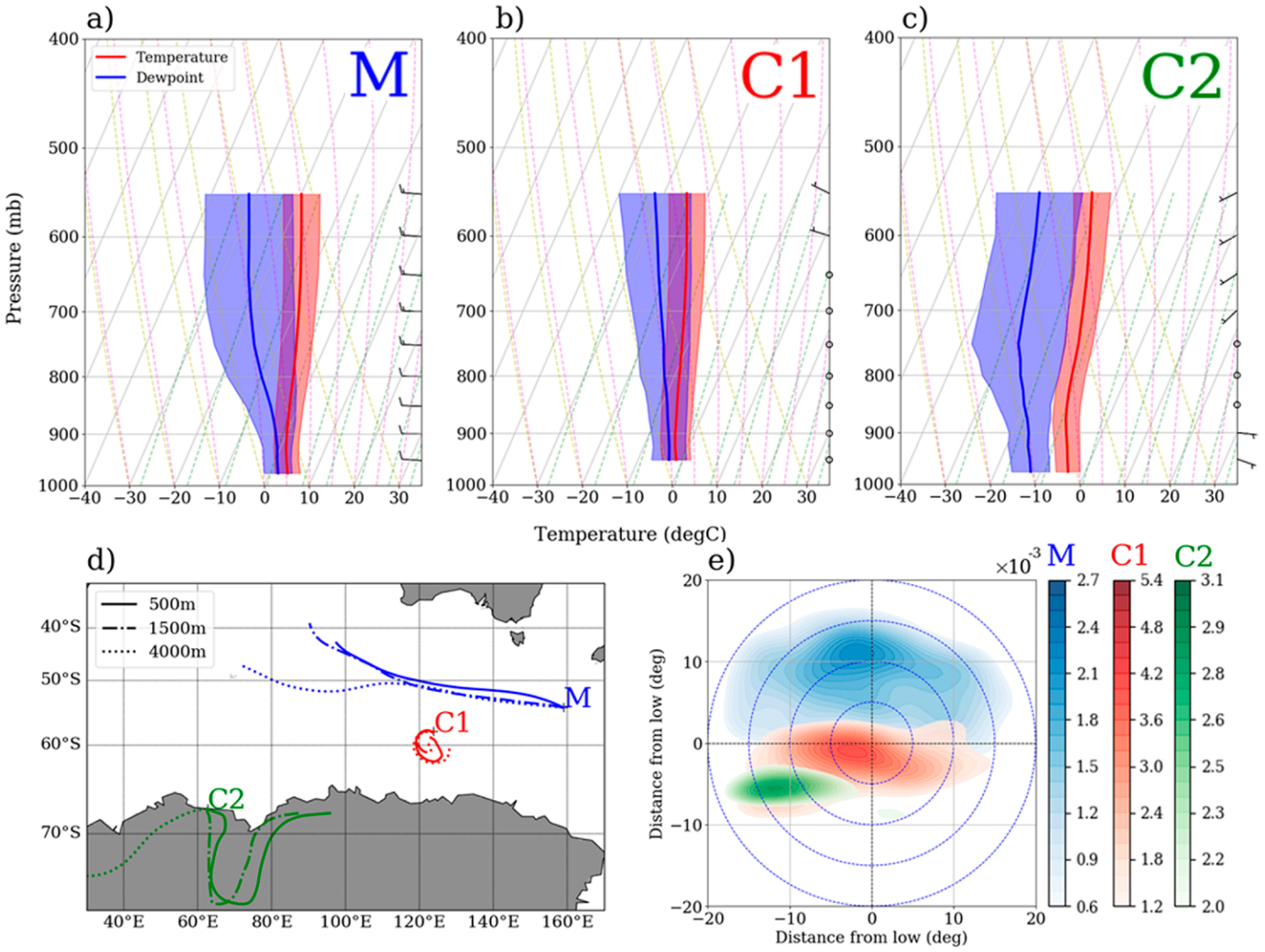

Fig. 18. (a)–(c) Mean profiles of temperature (red line), dewpoint temperature (blue line), and vector wind for the clusters M, C1, and C2, respectively, displayed as a skew *T*–log*P* diagram, with the shaded region indicating one standard deviation. (d) The 72-h HYSPLIT back trajectory for the nearest soundings to the centroid in each cluster M, C1, and C2, separately. The solid, dash–dotted, and dotted lines represent the tracks at 500, 1,500, and 4,000 m, respectively. (e) The frequency of occurrence composites of the sounding locations relative to the nearest cyclone centers, where concentric circles indicate distances of 5°, 10°, 15°, and 20° from the cyclone center.

droplet concentration N_c decreases steadily from >100 cm^{-3} as the R/V *Investigator* traveled south through the Tasman Sea to about 50 cm^{-3} as the ship passed into the latitudes of the Antarctic Circumpolar current. Cloud droplet concentration N_c increased by about a factor of 2 occurs on 29 January as the ship passed poleward of 64°S. Cloud droplet concentration N_c remained elevated while the R/V *Investigator* worked along the Antarctic shelf south of 60°S. Poor weather precluded retrievals until 13 February when N_c was again found to be in the 50 cm^{-3} range with the ship working back north of 60°S. Cloud droplet concentration N_c did not climb as rapidly with latitude moving northward toward Tasmania.

The daily mean N_c is correlated (r = 0.48) with daily averages of sulfate and particulate methanesulfonic acid (MSA) concentrations, but N_c is less well correlated with CCN at 0.65% super saturation measured at the surface (r = 0.38). It was also found (not shown) that N_c is

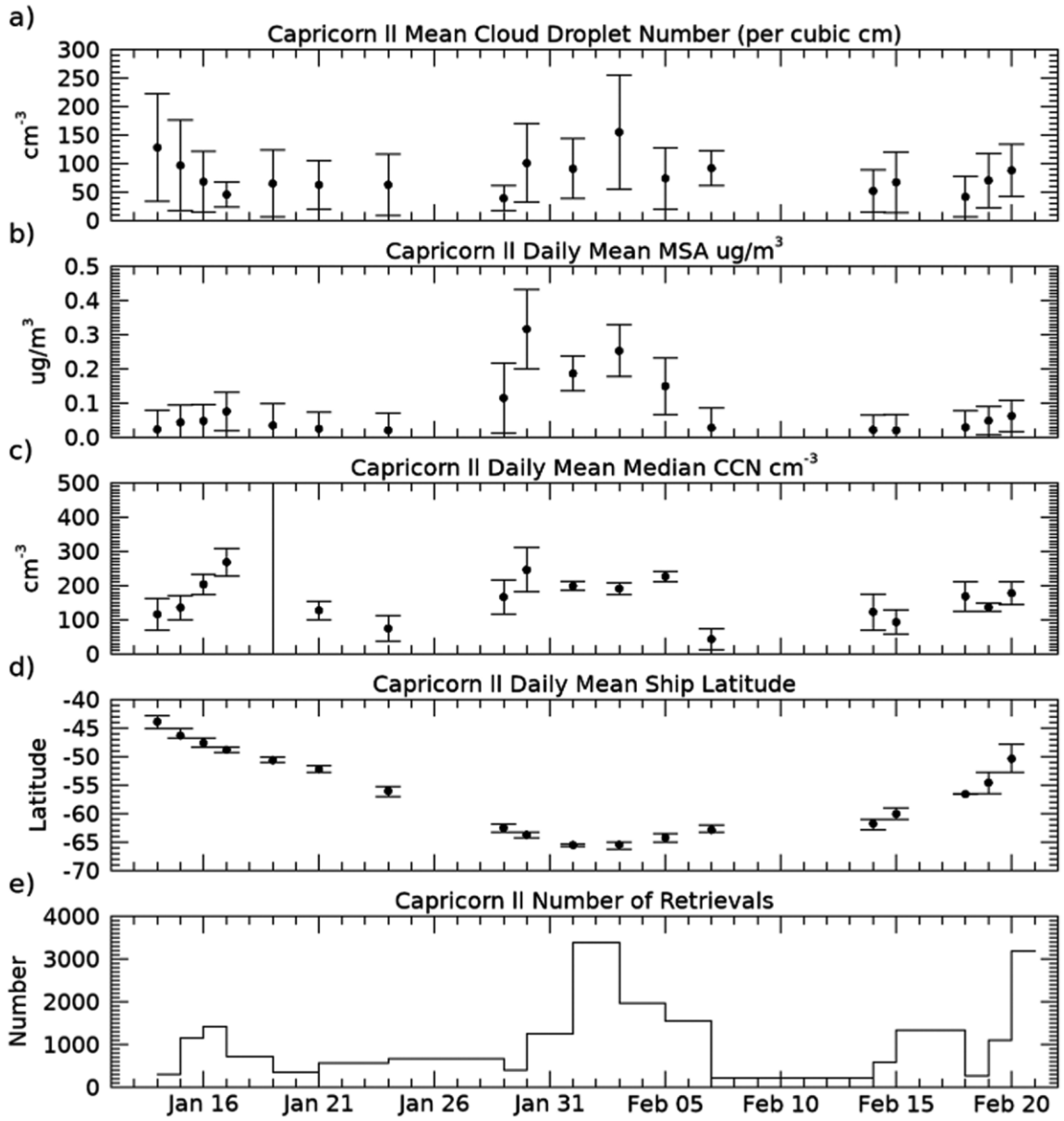

Fig. 19. Daily mean derived and observed properties from the R/V *Investigator* during Capricorn II. (a) Cloud droplet number concentrations N_c derived for nonprecipitating liquid clouds using combined radar reflectivity, microwave brightness temperature, and lidar attenuated backscatter. Error bars show the standard deviation of N_c during that 24-h period (only days with at least 200 30-s retrievals are shown), (b) particulate methanesulfonic (MSA) concentrations (μg m^{-3}), (c) CCN measured at 0.25% super saturation, (d) latitude of the ship on that day, and (e) number of N_c retrievals used in the N_c means and standard deviation in (a).

negatively correlated ($r = -0.51$) with chloride concentrations. What is reasonably striking in Fig. 19 is that N_c, MSA, and CCN all increase substantially poleward of 60°S. Because MSA is a marker of DMS oxidation, it is concluded that the higher CCN concentrations in this region are likely driven by the biologically productive latitudes along the Antarctic shelf. It is plausible that this effect is in line with previous observations by Humphries et al. (2016) where increased secondary aerosol formation was observed south of these latitudes.

Models test ubiquitous supercooled water and role of biological particles over SO. Global-scale, regional-scale, and process-scale modelers were entrained into the SO projects as they were designed. Scientists using the atmospheric component of NCAR's Community Earth System Model version 2 (CESM2) (Danabasoglu et al. 2020) and GFDL's AM4 (Zhao et al. 2018) global models participated. The Australian ACCESS model (Puri et al. 2013) was used for operational forecasting during SOCRATES, and its icing products were evaluated. Australian and U.S. groups ran the Weather Research and Forecast (WRF; Skamarock et al. 2005) regional model. A large-eddy simulation (LES) model (Atlas et al. 2020) was run with a very fine grid over small domains for selected cases, as was an idealized cloud-resolving model [Cloud Model 1 (CM1); Bryan and Fritsch 2002] for process-level studies. Table ES13 lists some modeling groups that participated in the projects, as well as the approximate grid resolution; additional details about the LES simulations are also included in the online supplement. Two particular foci of the modeling studies were to test hypotheses that (i) the GCMs/NWP models were too quickly glaciating clouds that are in reality persistent SLW clouds, and (ii) marine biogenic processes help sustain the natural aerosol population over the SO.

From the start, the modeling team proposed a nudged-meteorology strategy (e.g., Wu et al. 2017) to effectively compare the global model with aircraft or ship data in the synoptically active SO. As implemented, three-dimensional model fields of horizontal wind, temperature and surface pressure were nudged toward a global reanalysis with a 24-h relaxation time scale. The simulated humidity, cloud and aerosol fields freely evolve and can be usefully compared with in situ observations. Ideally, the temperature and wind fields from the nudged simulations and from the reanalysis to which they are being nudged should closely match corresponding observations. This was found to hold remarkably well. For instance, aircraft-measured temperatures were typically within 1 K of the reanalysis and within 2 K of the nudged GCMs. Figure 5 of Gettelman et al. (2020) shows the example of RF07, in which CAM6 is nudged to the MERRA2 reanalysis. Both MERRA2 and the ERA5 reanalysis used by the nudged AM4 are fine choices for the nudged-meteorology approach. ERA5, which input the G-V dropsonde data, was on average about 20% closer to SOCRATES-observed temperature and winds than MERRA2. In addition, the regular radiosonde observations made during MARCUS have been found to improve the forecast track of a midlatitude low pressure system (Sato et al. 2018).

Figures 10 and 14 of Gettelman et al. (2020) show examples of comparisons of nudged versions of CAM6 and its predecessor version CAM5 with aircraft cloud microphysical observations from SOCRATES RF07. These show that CAM6 correctly simulates a BL stratocumulus layer that is observed to be primarily supercooled liquid, while CAM5 incorrectly simulates the same cloud layer to mainly be ice. CAM6 is also able to represent the structure of the hydrometeor size distributions [Fig. 20, adapted from Fig. 9 of Gettelman et al. (2020)], but with biases remaining in the representation of the peak liquid size distribution, and in excessive warm rain. These detailed comparisons allow a new process understanding of weather and climate models from the in situ microphysical to the climate scale (Gettelman et al. 2020).

Both the NSF G-V used in SOCRATES and the R/V *Investigator* in CAPRICORN II gathered extensive vertically pointing lidar and 94-GHz cloud radar datasets that sampled entire atmospheric columns. Both the CAM6 and AM4 models include implementations of the COSP simulator (Bodas-Salcedo et al. 2011), which includes a 94-GHz radar simulator. This enables

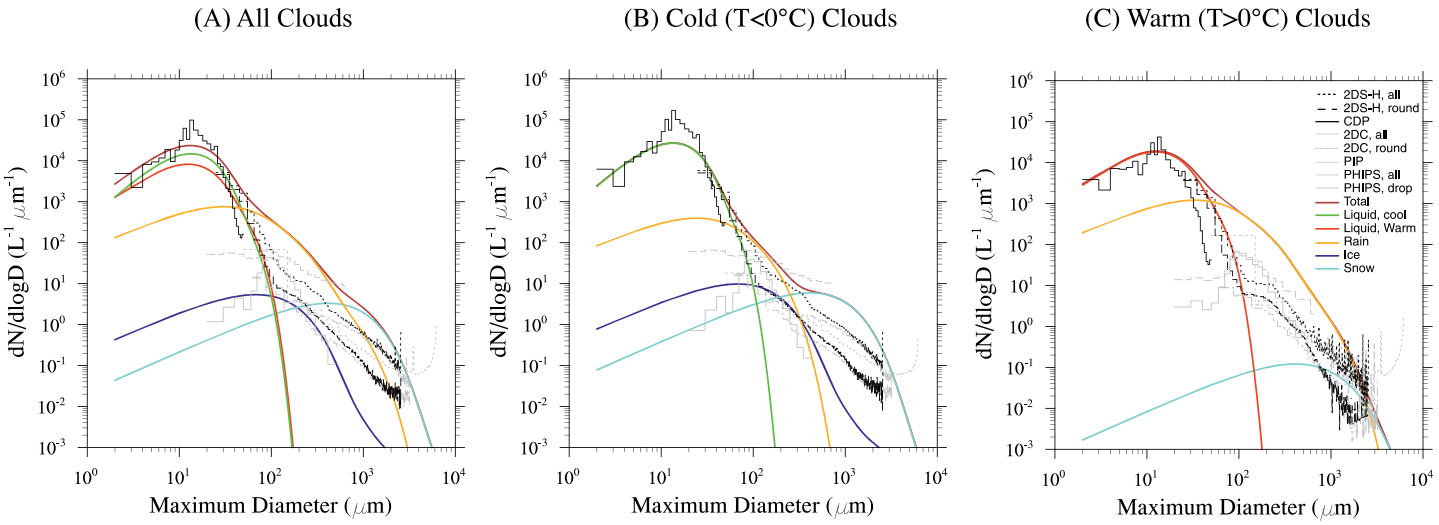

Fig. 20. Size distributions from observations (thin lines) and reconstructed model hydrometeor size distributions (thick colored lines) for low level clouds (p > 750 mb) as indicated in the legend. Cloud probe data shown as 2DS for all particles (black dotted), 2DS round particles (black dash), CDP (black solid), 2DC all (gray dash), 2DC round (gray dot–dash), PIP (gray dotted), PHIPS all (gray long dash), and PHIPS drop (gray solid). (a) All clouds, (b) cold clouds, and (c) warm clouds. Model is sampled along the flight track at aircraft altitude.

a comparison between these powerful remote sensing datasets and the nudged-meteorology GCMs, discussed at length by Zhou et al. (2021). Their Fig. 12 shows such a comparison with the R/V *Investigator* radar data for 1–15 February 2018. This is a sensitivity test of the model cloud microphysics and representation of precipitation. It shows CAM6 has good skill, while AM4 greatly underestimates snow reflectivity because its assumed snow particle size is too small. The ship radar often sampled precipitating clouds which the aircraft did not target (and which were often precluded by icing hazard), so it provides complementary information to the in situ data.

Summary and future work

Motivated by a pressing issue on the absorption of too much solar radiation over the Southern Ocean (SO) (due to problems simulating low-altitude supercooled liquid clouds) by leading climate and numerical weather prediction models, a coordinated multiagency effort consisting of four field campaigns was held in the time period of 2016–18. The experimental design, platforms, and instruments from four experiments have been summarized here: the ground-based Macquarie Island Cloud Radiation Experiment (MICRE) collecting information on surface aerosol properties in situ, and clouds, precipitation and radiation using remote sensors; the Clouds Aerosols Precipitation Radiation and Atmospheric Composition over the SO (CAPRICORN) I and II cruises of the R/V *Investigator* that collected aerosol, in situ and oceanographic measurements in situ and remotely; the Measurements of Aerosols, Radiation and Clouds over the Southern Ocean (MARCUS) campaign that collected in situ aerosol and remote sensing observations using instruments installed on the icebreaker RSV *Aurora Australis* as it made resupply voyages from Hobart to the Australian Antarctic stations and Macquarie Island; and the Southern Ocean Cloud Radiation Transport Experimental Study (SOCRATES) that collected data with the NSF–NCAR G-V aircraft in a north–south direction south of Hobart, Tasmania, to approximately 62°S. These data characterize the synoptically and seasonally varying vertical structure of the SO Bland free troposphere, including the properties of clouds and the variability and sources and sinks of aerosols, cloud condensation nuclei, and ice nucleating particles, to a much greater extent than was previously available.

The experiments were designed to be complementary in how they contribute to studies of processes, latitudinal variability, seasonal variability, validation of remote sensing retrievals, and model evaluation and improvement. MICRE gives a long seasonal record in a single location, CAPRICORN I and II give the most complete shipborne oceanographic, aerosol, and surface energy budget observations, MARCUS covers a longer seasonal cycle than CAPRICORN, and SOCRATES provides the detailed in situ observations that are required for process-oriented understanding. Combined these data represent the most comprehensive set of data collected on aerosols, clouds and precipitation over the SO over seasonal cycles, especially over cold sectors of extratropical cyclones and at latitudes below 60°S where climate model biases are largest. The related modeling studies tested hypotheses on the cloud processes that lead to the ubiquity of supercooled clouds and the marine biogenic processes that sustain the natural aerosol population over the SO.

Some first findings from the field campaigns addressing their overarching objectives have been presented here, and are being elaborated upon in several more focused scientific articles. Initial findings included that low clouds were responsible for nearly all the radiative biases in the Australian forecast model ACCESS and the presence of a pristine environment with numerous small and few large aerosols above cloud, highlighting the role of new particle formation in the troposphere and the long-range transport from continents. There is a dearth of INPs [much lower than suggested by much earlier measurements by Bigg (1973)], which is a significant factor leading to the ubiquitous presence of supercooled liquid water over the SO. Most INPs appear to have a biological source and better understanding of secondary ice nucleating processes related to these particles is needed. Further, there was a suggestion that the higher CCN concentrations south 60°S were likely driven by biologically productive latitudes along the Antarctic shelf, but that sea spray may have more important roles in other latitudinal bands. In the cold dry sectors of cyclones, supercooled liquid water with contents as high as about 0.8 g m^{-3} was observed in very thin layers at temperatures as low as −30°C and was frequently associated with the presence of narrow cloud-top generating cells. Evaluation of satellite datasets is ongoing, but early results suggest the CERES shortwave fluxes and imager-based (Himawari and MODIS) retrievals for low cloud microphysical properties for stratocumulus are reasonably good, and pointing toward ways in which retrievals of precipitation and cloud phase among other may quantities might be refined or improved. Finally, ongoing modeling and observations studies are examining how CCN properties are coupled with aerosol properties and meteorological conditions, in order to provide a process-oriented understanding that can be used to improve the performance of models at a variety of spatial and temporal scales.

In terms of the motivating goal, namely, the overprediction of solar radiation over the SO, the hypothesis that SLW is ubiquitous is confirmed. Although measurements verified that there was a dearth of INPs over the SO, the exact mechanisms by which SLW persists over the SO, and the interplay of aerosols, dynamics, and meteorology in this persistence are still somewhat uncertain. Now that all data have been processed and conditions over the SO have been characterized, integration of different datasets and comparison against models and satellite retrievals is proceeding rapidly, which should lead to a more integrated view of the abundance of supercooled water and its role in reflecting solar radiation to reduce the observed radiative bias.

Inevitably, the collected datasets have limitations with their temporal and spatial coverage. Use of the data to evaluate and improve satellite retrieval schemes will extend the impact of these SO datasets. Nonetheless, it will be advantageous to collect future aircraft and ship-based datasets over the SO. In order for future data to have the maximum impact, it could be desirable to use a Lagrangian approach to aircraft data collection rather than the Eulerian approach used during SOCRATES. Although the Eulerian approach was beneficial for characterizing the SO environment, a Lagrangian approach would allow for better understanding of

how clouds evolve over longer periods of time by tracing their evolution on subsequent days. In addition, a focus on the transition season where there is a greater variability in the strength of phytoplankton blooms, and the winter seasons where biological activity is low would allow for testing on hypotheses related to the impact of biogenic aerosol species and generally provide a more thorough understanding of seasonal differences. More comprehensive measurements of aerosol chemical properties as well as of cloud particles with sizes between 50 and 150 μm, perhaps through holographic probes, would also be beneficial. Nevertheless, the publicly available CAPRICORN, MICRE, MARCUS, and SOCRATES data significantly extend the availability of data on cloud, precipitation and aerosol properties over the SO, and will offer rich datasets for future studies.

Acknowledgments. This work was supported by the National Science Foundation (NSF) through Grants AGS-1628674 (GMM, RMR, SLT) and AGS-1762096 (GMM, RMR, SLT) and by the United States Department of Energy through Grant DE-SC0018626. CSB, RW, and ILM acknowledge NSF Grant AGS-1660609, and CSB and RLA acknowledge NSF Grant AGS-1660604. GCR and KJS acknowledge NSF Grant AGS-1660374. CHT acknowledges NSF Grant AGS-1660605. DT and BR acknowledge NSF Grant AGS-1660537. PJD, TCJH, and KAM acknowledge NSF Grant AGS-1660486 and DOE Grant DE-SC0018929. KAM acknowledges support by an NSF Graduate Research Fellowship under Grant 006784. JU was supported by the National Research Foundation of Korea (NRF) grant funded by the Korean government (MSIT) 2020R1A2C1013278 and by Basic Science Research Program through the NRF funded by the Ministry of Education (No. 2020R1A6A1A03044834). CM was supported primarily by the National Center for Atmospheric Research and received travel support from NSF AGS-1660486. YH acknowledges support from the Australian Research Council's DP150102894, DP190101362 and CE170100023 grants. SS acknowledges support from the Australian Research Council's DP150102894 and DP190101362 grants and the Australian Antarctic Division's AAD4340 grant. The material in the article is based upon work supported by the National Center for Atmospheric Research, which is a major facility sponsored by the NSF under Cooperative Agreement 1852977. The data were collected using NSF's Lower Atmosphere Observing Facilities, which are managed and operated by NCAR's Earth Observing Laboratory. The Australian Bureau of Meteorology's contribution to these studies was funded by the Australian government through the National Environmental Science Program (NESP) and the Australian Antarctic Partnership Program (AAPP). The efforts of the entire SOCRATES, MARCUS, MICRE, and CAPRICORN teams in collecting the high-quality datasets are appreciated. Technical, logistical, and ship support for MARCUS and MICRE were provided by the AAD through Australian Antarctic Science Projects 4431, 4292, and 4387, and we thank Steven Whiteside, Lloyd Symonds, Rick van den Enden, Peter de Vries, Chris Young, Chris Richards, Terry Egan, Nick Cartwright, and Ken Barrett for assistance. Logistical and financial support was provided for CAPRICORN by the Australian Marine National Facility. Anne Marie Rauker is acknowledged for assistance in INP data processing. Anne Perring is acknowledged for the use of her WIBS-4A during CAPRICORN II. Paul Selleck is acknowledged for his work with the ToF-ACSM during CAPRICORN II. Robyn Schofield also acknowledges support from the Australian Research Council's DP160101598, LE150100048, and CE170100023 grants. The SOCRATES principal investigators would like to thank the BoM Tasmanian regional Office for the excellent forecast support and weather briefings provided during the field campaign (with special thanks to Scott Carpentier, Michelle Hollister, Matthew Thomas, and Robert Schaap). We thank the Atmospheric Radiation Measurement (ARM) Program sponsored by the U.S. DOE, Office of Science, Office of Biological and Environmental Research, Climate and Environmental Science Division for their support. Any opinions, findings, and conclusions or recommendations expressed in this material are those of the author(s) and do not necessarily reflect the views of the funding agencies.

Data availability statement. Copies of all Atmospheric Radiation Measurement (ARM) Program instrument-level data collected during MARCUS and MICRE are permanently stored and available via the

ARM data archive (https://adc.arm.gov/). Data from AAD, BoM, and CSIRO instruments deployed alongside MARCUS and MICRE instrumentation are available from the Australian Antarctic Data Centre following registration. Copies of non-ARM instrument-level data and derived (multi-instrument) fields (such as cloud liquid water path and effective radius, precipitation particle type) will eventually be available through ARM archive as a primary investigator data (PI data). As of the time this article is being written, the processing of these data is not yet complete but are available at https://atmos.uw.edu/~roj/nobackup/MARCUS_and_MICRE/Datasets/. The author(s) wish to acknowledge the SOCRATES Project and the SOCRATES Data Archive Center at NCAR's Earth Observing Laboratory, https://data.eol.ucar.edu/master_lists/generated/socrates/. The CAPRICORN datasets are available on the CSIRO Data Access Portal at https://data.csiro.au/dap.

Appendix: Acronyms

A list of all the abbreviations used in the main text of the manuscript is provided here.

AA	RSV *Aurora Australis*
AAD	Australian Antarctic Division
AMF2	ARM Marine Facility 2
AR	Atmospheric river
ARM	Atmospheric Radiation Measurement
BL	Boundary layer
BoM	Australian Bureau of Meteorology
CALIPSO	*Cloud–Aerosol Lidar and Infrared Pathfinder Satellite Observations*
CAPRICORN	Clouds Aerosols Precipitation Radiation and Atmospheric Composition over the Southern Ocean
CCN	Cloud condensation nucleus
CDP	Cloud Droplet Probe
CERES	Clouds and the Earth's Radiant Energy System
CFAD	Contour frequency by altitude diagram
CFDC	Continuous flow diffusion chamber
CMIP5	Coupled Model Intercomparison Project phase 5
CSU	Colorado State University
DMS	Dimethyl sulfide
DOE	Department of Energy
DSD	Drop size distribution
ECMWF	European Centre for Medium-Range Weather Forecasting
ERA5	ECMWF Re-Analysis 5
FBAP	Fluorescent biological aerosol particle
FT	Free troposphere
GCM	General circulation model
GPCP	Global Precipitation Climatology Project
GPM	Global Precipitation Measurement
G-V	Gulfstream V
HCR	HIAPER Cloud Radar
HGF	Hygroscopic growth factor
HIAPER	High-Performance Instrumented Airborne Platform for Environmental Research
HSRL	High Spectral Resolution Lidar
HYSPLIT	Hybrid Single-Particle Lagrangian Integrated Trajectory Model
INP	Ice nucleating particle
IS	Ice spectrometer
ITCZ	Intertropical convergence zone
JAXA	Japan Aerospace Exploration Agency

LW	Longwave
MARCUS	Measurements of Aerosols, Radiation and Clouds over the Southern Ocean
MBL	Marine boundary layer
MICRE	Macquarie Island Cloud Radiation Experiment
MNF	Australian Marine National Facility
MSA	Methanesulfonic acid
N_a	Aerosol concentration
N_c	Cloud droplet number concentration
NASA	National Aeronautics and Space Administration
NCAR	National Center for Atmospheric Research
NH	Northern Hemisphere
NOAA	National Oceanographic and Atmospheric Administration
NSF	National Science Foundation
NWP	Numerical weather prediction
PHIPS	Particle Habit Imaging and Polar Scattering probe
PIP	Precipitation Imaging Probe
RF	Research flight
RPF	Recent particle formation
SLW	Supercooled liquid water
SO	Southern Ocean
SOCRATES	Southern Ocean Cloud Radiation Aerosol Transport Experimental Study
SST	Sea surface temperature
STEM	Scanning transmission electron microscopy
SW	Shortwave
T	Temperature
UHSAS	Ultra High Sensitivity Aerosol Sampler
VOC	Volatile organic carbon
WIBS-4	Waveband Integrated Bioaerosol Sensor 4
WRF	Weather Research and Forecasting Model
2DC	Two-Dimensional Cloud Probe
2DS	Two-Dimensional Stereo Probe
λ	Wavelength of radiation

References

Ahn, E., Y. Huang, T. H. Chubb, D. Baumgardner, P. Isaac, M. de Hoog, S. T. Siems, and M. Manton, 2017: In situ observations of wintertime low-altitude clouds over the Southern Ocean. *Quart. J. Roy. Meteor. Soc.*, **143**, 1381–1394, https://doi.org/10.1002/qj.3011.

Andreae, M. O., W. Elbert, and S. J. Demora, 1995: Biogenic sulfur emissions and aerosols over the tropical South Atlantic: 3. Atmospheric dimethylsulfide, aerosols and cloud condensation nuclei. *J. Geophys. Res.*, **100**, 11 335–11 356, https://doi.org/10.1029/94JD02828.

Andreas, A., M. Dooraghi, A. Habte, M. Kutchenreiter, I. Reda, and M. Sengupta, 2018: Solar infrared radiation station (SIRS), sky radiation (SKYRAD), ground radiation (GNDRAD), and broadband radiometer station (BRS) instrument handbook. U.S. Department of Energy Doc. DOE/SC-ARM-TR-025, 58 pp., www.arm.gov/publications/tech_reports/handbooks/sirs_handbook.pdf.

Angulo-Martinez, M., S. Begueria, B. Latorre, and M. Fernandez-Raga, 2018: Comparison of precipitation measurements by OTT Parsivel2 and Thies LPM optical disdrometers. *Hydrol. Earth Syst. Sci.*, **22**, 2811–2837, https://doi.org/10.5194/hess-22-2811-2018.

Atlas, R. L., C. S. Bretherton, and P. N. Blossey, 2020: How well do high and low resolution models represent observed boundary layer structures and low clouds over the summertime Southern Ocean? *J. Adv. Model. Earth Syst.*, **12**, e2020MS002205, https://doi.org/10.1029/2020MS002205.

Ayers, G. P., and J. L. Gras, 1991: Seasonal relationship between cloud condensation nuclei and aerosol methanesulfonate in marine air. *Nature*, **353**, 834–835, https://doi.org/10.1038/353834a0.

Bates, T. S., and Coauthors, 1998a: Processes controlling the distribution of aerosol particles in the lower marine boundary layer during the First Aerosol Characterization Experiment (ACE-1). *J. Geophys. Res.*, **103**, 16 369–16 383, https://doi.org/10.1029/97JD03720.

——, B. J. Huebert, J. L. Gras, F. B. Griffiths, and P. A. Durkee, 1998b: International Global Atmospheric Chemistry (IGAC) project's first Aerosol Characterization Experiment (ACE 1): Overview. *J. Geophys. Res.*, **103**, 16 297–16 318, https://doi.org/10.1029/97JD03741.

——, P. K. Quinn, D. S. Covert, D. J. Coffman, J. E. Johnson, and A. Wiedensohler, 2000: Aerosol physical properties and processes in the lower marine boundary layer: A comparison of shipboard sub-micron data from ACE 1 and ACE 2. *Tellus*, **52**, 258–272, https://doi.org/10.3402/tellusb.v52i2.16104.

Bigg, E. K., 1973: Ice nucleus concentrations in remote areas. *J. Atmos. Sci.*, **30**, 1153–1157, https://doi.org/10.1175/1520-0469(1973)030<1153:INCIRA>2.0.CO;2.

Bodas-Salcedo, A., and Coauthors, 2011: COSP: Satellite simulation software for model assessment. *Bull. Amer. Meteor. Soc.*, **92**, 1023–1043, https://doi.org/10.1175/2011BAMS2856.1.

——, and Coauthors, 2014: Origins of the solar radiation biases over the Southern Ocean in CFMIP2 models. *J. Climate*, **27**, 41–56, https://doi.org/10.1175/JCLI-D-13-00169.1.

——, T. Andrews, A. V. Karmalkar, and M. A. Ringer, 2016: Cloud liquid water path and radiative feedbacks over the Southern Ocean. *Geophys. Res. Lett.*, **43**, 10 938–10 946, https://doi.org/10.1002/2016GL070770.

Boers, R., J. B. Jensen, P. B. Krummel, and H. Gerber, 1996: Microphysical and short-wave radiative structure of wintertime stratocumulus clouds over the Southern Ocean. *Quart. J. Roy. Meteor. Soc.*, **122**, 1307–1339, https://doi.org/10.1002/qj.49712253405.

——, ——, and ——, 1998: Microphysical and short-wave radiative structure of stratocumulus clouds over the Southern Ocean: Summer results and seasonal differences. *Quart. J. Roy. Meteor. Soc.*, **124**, 151–168, https://doi.org/10.1002/qj.49712454507.

Bryan, G. H., and J. M. Fritsch, 2002: A benchmark simulation for moist nonhydrostatic numerical models. *Mon. Wea. Rev.*, **130**, 2917–2928, https://doi.org/10.1175/1520-0493(2002)130<2917:ABSFMN>2.0.CO;2.

Burrows, S. M., C. Hoose, U. Pöschl, and M. G. Lawrence, 2013: Ice nuclei in marine air: Biogenic particles or dust? *Atmos. Chem. Phys.*, **13**, 245–267, https://doi.org/10.5194/acp-13-245-2013.

Carslaw, K. S., and Coauthors, 2013: Large contribution of natural aerosols to uncertainty in indirect forcing. *Nature*, **503**, 67–71, https://doi.org/10.1038/nature12674.

Ceppi, P., M. D. Zelinka, and D. L. Hartmann, 2014: The response of the Southern Hemispheric eddy-driven jet to future changes in shortwave radiation in CMIP5. *Geophys. Res. Lett.*, **41**, 3244–3250, https://doi.org/10.1002/2014GL060043.

Cho, H.-M., and Coauthors, 2015: Frequency and causes of failed MODIS cloud property retrievals for liquid phase clouds over global oceans. *J. Geophys. Res. Atmos.*, **120**, 4132–4154, https://doi.org/10.1002/2015JD023161.

Choi, Y. S., C. H. Ho, S. W. Kim, and R. S. Lindzen, 2010: Observational diagnosis of cloud phase in the winter Antarctic atmosphere for parameterizations in climate models. *Adv. Atmos. Sci.*, **27**, 1233–1245, https://doi.org/10.1007/s00376-010-9175-3.

Chubb, T. H., J. B. Jensen, S. T. Siems, and M. J. Manton, 2013: In situ observations of supercooled liquid clouds over the Southern Ocean during the HIAPER Pole-to-Pole Observation campaigns. *Geophys. Res. Lett.*, **40**, 5280–5285, https://doi.org/10.1002/grl.50986.

——, Y. Huang, J. Jensen, T. Campos, S. Siems, and M. Manton, 2016: Observations of high droplet number concentrations in Southern Ocean boundary layer clouds. *Atmos. Chem. Phys.*, **16**, 971–987, https://doi.org/10.5194/acp-16-971-2016.

Clarke, A. D., 1993: Atmospheric nuclei in the Pacific midtroposphere: Their nature, concentration, and evolution. *J. Geophys. Res.*, **98**, 20 633–20 647, https://doi.org/10.1029/93JD00797.

——, J. L. Varner, F. Eisele, R. L. Mauldin, D. Tanner, and M. Litchy, 1998: Particle production in the remote marine atmosphere: Cloud outflow and subsidence during ACE 1. *J. Geophys. Res.*, **103**, 16 397–16 409, https://doi.org/10.1029/97JD02987.

Clement, C. F., I. J. Ford, C. H. Twohy, A. Weinheimer, and T. Campos, 2002: Particle production in the outflow of a midlatitude storm. *J. Geophys. Res.*, **107**, 4559, https://doi.org/10.1029/2001JD001352.

Cober, S. G., and G. A. Isaac, 2012: Characterization of aircraft icing environments with supercooled large drops for application to commercial aircraft certification. *J. Appl. Meteor. Climatol.*, **51**, 265–284, https://doi.org/10.1175/JAMC-D-11-022.1.

Covert, D. S., V. N. Kapustin, P. K. Quinn, and T. S. Bates, 1992: New particle formation in the marine boundary layer. *J. Geophys. Res.*, **97**, 20 581–20 589, https://doi.org/10.1029/92JD02074.

——, ——, T. S. Bates, and P. K. Quinn, 1996: Physical properties of marine boundary layer aerosol particles of the mid-Pacific in relation to sources and meteorological transport. *J. Geophys. Res.*, **101**, 6919–6930, https://doi.org/10.1029/95JD03068.

D'Alessandro, J. J., M. Diao, C. Wu, X. Liu, J. B. Jensen, and B. B. Stephens, 2019: Cloud phase and relative humidity distributions over the Southern Ocean in austral summer based on in situ observations and CAM5 simulations. *J. Climate*, **32**, 2781–2805, https://doi.org/10.1175/JCLI-D-18-0232.1.

Danabasoglu, G., and Coauthors, 2020: The Community Earth System Model version 2 (CESM2). *J. Adv. Model. Earth Syst.*, **12**, e2019MS001916, https://doi.org/10.1029/2019MS001916.

Delanoë, J., and R. Hogan, 2010: Combined CloudSat-CALIPSO-MODIS retrievals of the properties of ice clouds. *J. Geophys. Res.*, **115**, D00H29, https://doi.org/10.1029/2009JD012346.

FAA, 2015: Airplane and engine certification requirements in supercooled large drop, mixed phase and ice crystal icing conditions; final rule. U.S. Code of Federal Regulations Title 14, Parts 25 and 33, 34 pp.

Flato, G., and Coauthors, 2013: Evaluation of climate models. *Climate Change 2013: The Physical Science Basis*, T. F. Stocker et al., Eds., Cambridge University Press, 741–882, https://doi.org/10.1017/CBO9781107415324.020.

Gettelman, A., and Coauthors, 2020: Simulating observations of Southern Ocean clouds and implications for climate. *J. Geophys. Res. Atmos.*, **125**, e2020JD032619, https://doi.org/10.1029/2020JD032619.

Ghan, S. J., and Coauthors, 2013: A simple model of global aerosol indirect effects. *J. Geophys. Res. Atmos.*, **118**, 6688–6707, https://doi.org/10.1002/jgrd.50567.

Gras, J. L., and M. Keywood, 2017: Cloud condensation nuclei over the Southern Ocean: wind dependence and seasonal cycles. *Atmos. Chem. Phys.*, **17**, 4419–4432, https://doi.org/10.5194/acp-17-4419-2017.

Grecu, M., W. S. Olson, S. J. Munchak, S. Ringerud, L. Liao, Z. Haddad, B. L. Kelley, and S. F. McLaughlin, 2016: The GPM combined algorithm. *J. Atmos. Oceanic Technol.*, **33**, 2225–2245, https://doi.org/10.1175/JTECH-D-16-0019.1.

Grosvenor, D. P., and R. Wood, 2014: The effect of solar zenith angle on MODIS cloud optical and microphysical retrievals within marine liquid water clouds. *Atmos. Chem. Phys.*, **14**, 7291–7321, https://doi.org/10.5194/acp-14-7291-2014.

——, T. W. Choularton, T. Lachlan-Cope, M. W. Gallagher, J. Crosier, K. N. Bower, R. S. Ladkin, and J. R. Dorsey, 2012: In-situ aircraft observations of ice concentrations within clouds over the Antarctic Peninsula and Larsen ice shelf. *Atmos. Chem. Phys.*, **12**, 11 275–11 294, https://doi.org/10.5194/acp-12-11275-2012.

Hande, L. B., S. T. Siems, M. J. Manton, and D. Belusic, 2012: Observations of wind shear over the Southern Ocean. *J. Geophys. Res.*, **117**, D12206, https://doi.org/10.1029/2012JD017488.

Hartery, S., D. W. Toohey, L. Revell, K. Sellegri, P. Kuma, M. Harvey, and A. J. McDonald, 2020: Constraining the surface flux of sea spray particles from the Southern Ocean. *J. Geophys. Res. Atmos.*, **125**, e2019JD032026, https://doi.org/10.1029/2019JD032026.

Hegg, D. A., R. J. Ferek, P. V. Hobbs, and L. F. Radke, 1991: Dimethyl sulfide and cloud condensation nucleus correlations in the northeast Pacific Ocean. *J. Geophys. Res.*, **96**, 13 189–13 191, https://doi.org/10.1029/91JD01309.

Heidinger, A. K., 2011: ABI cloud height. NOAA/NESDIS Center for Satellite Applications and Research Algorithm Theoretical Basis Doc., version 3, 77 pp., www.star.nesdis.noaa.gov/goesr/docs/ATBD/Cloud_Height.pdf.

Hinkelman, L. and R. Marchand, 2020: Evaluation of CERES and CloudSat surface radiative fluxes over the Southern Ocean. *Earth Space Sci.*, **7**, e2020EA001224, https://doi.org/10.1029/2020EA001224.

Holben, B. N., and Coauthors, 1998: AERONET—A federated instrument network and data archive for aerosol characterization. *Remote Sens. Environ.*, **66**, 1–16, https://doi.org/10.1016/S0034-4257(98)00031-5.

Holton, J. R., and G. J. Hakim, 2013: *An Introduction to Dynamic Meteorology*. 5th ed. Academic Press, 552 pp.

Hoose, C., J. E. Kristjánsson, T. Iversen, A. Kirkevåg, Ø. Seland, and A. Gettelman, 2009: Constraining cloud droplet number concentration in GCMs suppresses the aerosol indirect effect. *Geophys. Res. Lett.*, **36**, L12807, https://doi.org/10.1029/2009GL038568.

Hu, Y., S. Rodier, K. Xu, W. Sun, J. Huang, B. Lin, P. Zhai, and D. Josset, 2010: Occurrence, liquid water content, and fraction of supercooled water clouds from combined CALIOP/IIR/MODIS measurements. *J. Geophys. Res.*, **115**, D00H34, https://doi.org/10.1029/2009JD012384.

Huang, Y., S. T. Siems, M. J. Manton, L. B. Hande, and J. M. Haynes, 2012a: The structure of low-altitude clouds over the Southern Ocean as seen by CloudSat. *J. Climate*, **25**, 2535–2546, https://doi.org/10.1175/JCLI-D-11-00131.1.

——, ——, ——, A. Protat, and J. Delanoë, 2012b: A study on the low-altitude clouds over the Southern Ocean using the DARDAR-MASK. *J. Geophys. Res.*, **117**, D18204, https://doi.org/10.1029/2012JD017800.

——, A. Protat, S.T. Siems and M.J. Manton, 2015a: A-Train observations of maritime midlatitude storm-track cloud systems: Comparing the Southern Ocean against the North Atlantic. *J. Climate*, **28**, 1920–1939, https://doi.org/10.1175/JCLI-D-14-00169.1.

——, C. N. Franklin, S. T. Siems, M. J. Manton, T. Chubb, A. Lock, S. Alexander, and A. Klekociuk, 2015b: Evaluation of boundary-layer cloud forecasts over the Southern Ocean in a limited-area numerical weather prediction system using in situ, space-borne and ground-based observations. *Quart. J. Roy. Meteor. Soc.*, **141**, 2259–2276, https://doi.org/10.1002/qj.2519.

——, S. T. Siems, M. J. Manton, D. Rosenfeld, R. Marchand, G. M. McFarquhar and A. Protat, 2016: What is the role of Sea Surface Temperature in Modulating Cloud and Precipitation Properties over the Southern Ocean? *J. Climate*, **29**, 7453–7464, https://doi.org/10.1175/JCLI-D-15-0768.1.

——, T. H. Chubb, D. Baumgardner, M. deHoog, S. T. Siems, and M. J. Manton, 2017: Evidence for secondary ice production in Southern Ocean open cellular convection. *Quart. J. Roy. Meteor. Soc.*, 143, 1685–1703, https://doi.org/10.1002/qj.3041.

——, M. Manton, S. Siems, A. Protat, L. Majewskic, and H. Nguyen, 2019: Evaluating Himawari-8 cloud products using shipborne and CALIPSO observations: Cloud-top height and cloud-top temperature. *J. Atmos. Oceanic Technol.*, **36**, 2327–2347, https://doi.org/10.1175/JTECH-D-18-0231.1.

Hudson, J. G., Y. Xie, and S. S. Yum, 1998: Vertical distribution of cloud condensation nuclei spectra over the summertime Southern Ocean. *J. Geophys. Res.*, **103**, 16 609–16 624, https://doi.org/10.1029/97JD03438.

Humphries, R. S., and Coauthors, 2015: Boundary layer new particle formation over East Antarctic sea ice—Possible Hg driven nucleation? *Atmos. Chem. Phys.*, **15**, 13 339–13 364, https://doi.org/10.5194/acp-15-13339-2015.

——, A. R. Klekociuk, R. Schofield, M. D. Keywood, J. Ward, and S. R. Wilson, 2016: Unexpectedly high ultrafine aerosol concentrations above East Antarctic sea ice. *Atmos. Chem. Phys.*, **16**, 2185–2206, https://doi.org/10.5194/acp-16-2185-2016.

Hwang, Y.-T., and D. M. M. Frierson, 2013: Link between the double-intertropical convergence zone problem and cloud biases over the Southern Ocean. *Proc. Natl. Acad. Sci. USA*, **110**, 4935–4940, https://doi.org/10.1073/pnas.1213302110.

IPCC, 2013: *Climate Change 2013: The Physical Science Basis*. T. F. Stocker et al., Eds., Cambridge University Press, 1535 pp.

Kanitz, T., P. Seifert, A. Ansmann, R. Engelmann, D. Althausen, C. Casiccia, and E.G. Rohwer, 2011: Contrasting the impact of aerosols at northern and southern midlatitudes on heterogeneous ice formation. *Geophys. Res. Lett.*, **38**, L17802, https://doi.org/10.1029/2011GL048532.

Kay, J. E., C. Wall, V. Yettella, B. Medeiros, C. Hannay, P. Caldwell, and C. Bitz, 2016: Global climate impacts of fixing the Southern Ocean shortwave radiation bias in the Community Earth System Model (CESM). *J. Climate*, **29**, 4617–4636, https://doi.org/10.1175/JCLI-D-15-0358.1.

Klekociuk, A. R., W. J. R. French, S. P. Alexander, P. Kuma, and A. J. McDonald, 2020a: The state of the atmosphere in the 2016 southern Kerguelen Axis campaign region. *Deep-Sea Res. II*, **174**, https://doi.org/10.1016/j.dsr2.2019.02.001.

——, D. J. Ottaway, A. D. MacKinnon, I. M. Reid, L. V. Twigger, and S. P. Alexander, 2020b: Australian lidar measurements of aerosol layers associated with the 2015 Calbuco eruption. *Atmosphere*, **11**, 124, https://doi.org/10.3390/atmos11020124.

Klepp, C., and Coauthors, 2018: OceanRAIN, a new in-situ shipboard global ocean surface-reference dataset of all water cycle components. *Sci. Data*, **5**, 180122, https://doi.org/10.1038/sdata.2018.122.

Korolev, A., and Coauthors, 2017: Mixed-phase clouds: Progress and challenges. *Ice Formation and Evolution in Clouds and Precipitation: Measurement and Modeling Challenges, Meteor. Monogr.*, No. 58, Amer. Meteor. Soc., https://doi.org/10.1175/AMSMONOGRAPHS-D-17-0001.1.

——, and Coauthors, 2020: A new look at the environmental conditions favorable to secondary ice production. *Atmos. Chem. Phys.*, **20**, 1391–1429, https://doi.org/10.5194/acp-20-1391-2020.

Kulmala, M., H. Vehkamäki, T. Petäjä, M. Dal Maso, A. Lauri, V.-M. Kerminen, W. Birmili, and P. H. McMurry, 2004: Formation and growth rates of ultrafine atmospheric particles: A review of observations. *J. Aerosol Sci.*, **35**, 143–176, https://doi.org/10.1016/j.jaerosci.2003.10.003.

Kuma, P., and Coauthors, 2020: Evaluation of Southern Ocean cloud in the HadGEM3 general circulation model and MERRA-2 reanalysis using ship-based observations. *Atmos. Chem. Phys.*, **20**, 6607–6630, https://doi.org/10.5194/acp-20-6607-2020.

Lang, F., Y. Huang, S. T. Siems, and M. J. Manton, 2018: Characteristics of the marine atmospheric boundary layer over the Southern Ocean in response to the synoptic forcing. *J. Geophys. Res. Atmos.*, **123**, 7799–7820, https://doi.org/10.1029/2018JD028700.

Lim, E.-P., and I. Simmonds, 2007: Southern Hemisphere winter extratropical cyclone characteristics and vertical organization observed with the ERA-40 reanalysis data in 1979–2001. *J. Climate*, **20**, 2675–2690, https://doi.org/10.1175/JCLI4135.1.

Mace, G. G., and A. Protat, 2018: Clouds over the Southern Ocean as observed from the R/V Investigator during CAPRICORN. Part II: The properties of nonprecipitating stratocumulus. *J. Appl. Meteor. Climatol.*, **57**, 1805–1823, https://doi.org/10.1175/JAMC-D-17-0195.1.

——, Q. Zhang, M. Vaughan, R. Marchand, G. Stephens, C. Trepte, and D. Winker, 2009: A description of hydrometeor layer occurrence statistics derived from the first year of merged CloudSat and CALIPSO data. *J. Geophys. Res.*, **114**, D00A26, https://doi.org/10.1029/2007JD009755.

Marchand, R., and Coauthors, 2014: The Southern Ocean Clouds, Radiation Aerosol Transport Experimental Study (SOCRATES). SOCRATES Planning Team Doc., 40 pp., https://atmos.uw.edu/~roj/nobackup/Southern_Ocean_Workshop_2014/Southern_Ocean_Workshop_2014_White_Paper.pdf.

McCluskey, C. S., and Coauthors, 2018a: A mesocosm double feature: Insights into the chemical makeup of marine ice nucleating particles. *J. Atmos. Sci.*, **75**, 2405–2423, https://doi.org/10.1175/JAS-D-17-0155.1.

——, and Coauthors, 2018b: Observations of ice nucleating particles over Southern Ocean waters. *Geophys. Res. Lett.*, **45**, 11 989–11 997, https://doi.org/10.1029/2018GL079981.

——, and Coauthors, 2018c: Marine and terrestrial organic ice nucleating particles in pristine marine to continentally-influenced northeast Atlantic air masses. *J. Geophys. Res. Atmos.*, **123**, 6196–6212, https://doi.org/10.1029/2017JD028033.

——, P. J. DeMott, P.-L. Ma, and S. M. Burrows, 2019: Numerical representations of marine ice-nucleating particles in remote marine environments evaluated against observations. *Geophys. Res. Lett.*, **46**, 7838–7847, https://doi.org/10.1029/2018GL081861.

McCoy, D. T., S. M. Burrows, R. Wood, D. P. Grosvenor, S. M. Elliott, P. L. Ma, P. J. Rasch, and D. L. Hartmann, 2015: Natural aerosols explain seasonal and spatial patterns of Southern Ocean cloud albedo. *Sci. Adv.*, **1**, e1500157, https://doi.org/10.1126/sciadv.1500157.

McCoy, I. L., C. S. Bretherton, R. Wood, C. H. Twohy, A. Gettleman, C. G. Bardeen and D. W. Toohey, 2021: Influences of recent particle formation on Southern Ocean aerosol variability and low cloud properties. *J. Geophys. Res. Atmos.*, **126**, e2020JD033529, https://doi.org/10.1029/2020JD033529.

McFarquhar, G. M., and Coauthors, 2011: Indirect and Semi-Direct Aerosol Campaign (ISDAC): The impact of arctic aerosols on clouds. *Bull. Amer. Meteor. Soc.*, **92**, 183–201, https://doi.org/10.1175/2010BAMS2935.1.

——, J. A. Finlon, D. M. Stechman, W. Wu, R. C. Jackson, and M. Freer, 2018: University of Illinois/Oklahoma optical array probe (OAP) processing software. Zenodo, https://doi.org/10.5281/zenodo.1285968.

McInnes, L. M., D. Covert, P. K. Quinn, and M. S. Germani, 1994: Measurements of chloride depletion and sulfur enrichment in individual sea-salt particles collected from the remote marine boundary layer. *J. Geophys. Res.*, **99**, 8257–8268, https://doi.org/10.1029/93JD03453.

Morrison, A. E., S. T. Siems, and M. J. Manton, 2011: A three-year climatology of cloud-top phase over the Southern Ocean and North Pacific. *J. Climate*, **24**, 2405–2418, https://doi.org/10.1175/2010JCLI3842.1.

Mossop, S. C., 1970: Concentration of ice crystals in clouds. *Bull. Amer. Meteor. Soc.*, **51**, 474–479, https://doi.org/10.1175/1520-0477(1970)051<0474:COICIC>2.0.CO;2.

Naud, C. M., J. F. Booth, and A. D. Del Genio, 2014: Evaluation of ERA-Interim and MERRA cloudiness in the Southern Ocean. *J. Climate,* **27**, 2019–2124, https://doi.org/10.1175/JCLI-D-13-00432.1.

Noh, Y.-J., S. D. Miller, A. K. Heidinger, G. G. Mace, A. Protat, and S. P. Alexander, 2019: Satellite-based detection of daytime supercooled liquid-topped mixed-phase clouds over the Southern Ocean using the Advanced Himawari Imager. *J. Geophys. Res. Atmos.*, **124**, 2677–2701, https://doi.org/10.1029/2018JD029524.

Pavolonis, M. J., 2010: GOES-R Advanced Baseline Imager (ABI) algorithm theoretical basis document for cloud type and cloud phase, version 2.0. NOAA NESDIS Center for Satellite Applications and Research Algorithm Theoretical Basis Doc., 86 pp., www.star.nesdis.noaa.gov/goesr/docs/ATBD/Cloud_Phase.pdf.

Pirjola, L., C. D. O'Dowd, I. M. Brooks, and M. Kulmala, 2000: Can new particle formation occur in the clean marine boundary layer? *J. Geophys. Res.*, **105**, 26 531–26 546, https://doi.org/10.1029/2000JD900310.

Plummer, D. M., G. M. McFarquhar, R. M. Rauber, B. F. Jewett, and D. Leon, 2014: Structure and statistical analysis of the microphysical properties of generating cells in the comma-head region of continental winter cyclones. *J. Atmos. Sci.*, **71**, 4181–4203, https://doi.org/10.1175/JAS-D-14-0100.1.

Protat, A., S. A. Young, L. Rikus, and M. Whimpey, 2014: Evaluation of the hydrometeor frequency of occurrence in a limited-area numerical weather prediction system using near real-time CloudSat–CALIPSO observations. *Quart. J. Roy. Meteor. Soc.*, **140**, 2430–2443, https://doi.org/10.1002/qj.2308.

——, E. Schulz, L. Rikus, Z. Sun, and Y. Xiao, 2017: Shipborne observations of the radiative effect of Southern Ocean clouds. *J. Geophys. Res. Atmos.*, **122**, 318–328, https://doi.org/10.1002/2016JD026061.

——, C. Klepp, V. Louf, W. Petersen, S. P. Alexander, A. Barros, and G. G. Mace, 2019a: The latitudinal variability of oceanic rainfall properties and its implication for satellite retrievals. Part I: The latitudinal variability of drop size distribution properties. *J. Geophys. Res. Atmos.*, **124**, 13 291–13 311, https://doi.org/10.1029/2019JD031010.

——, ——, ——, ——, ——, ——, and ——, 2019b: The latitudinal variability of oceanic rainfall properties and its implication for satellite retrievals. Part II: The relationships between radar observables and drop size distribution parameters. *J. Geophys. Res. Atmos.*, **124**, 13 312–13 324, https://doi.org/10.1029/2019JD031011.

Puri, K., and Coauthors, 2013: Implementation of the initial ACCESS numerical weather prediction system. *Aust. Meteor. Oceanogr. J.*, **63**, 265–284, https://doi.org/10.22499/2.6302.001.

Quinn, P. K., D. J. Coffman, J. E. Johnson, L. M. Upchurch, and T. S. Bates, 2017: Small fraction of marine cloud condensation nuclei made up of sea spray aerosol. *Nat. Geosci.*, **10**, 674–679, https://doi.org/10.1038/ngeo3003.

Read, K. A., and Coauthors, 2008: DMS and MSA measurements in the Antarctic boundary layer: Impact of BrO on MSA production. *Atmos. Chem. Phys.*, **8**, 2985–2997, https://doi.org/10.5194/acp-8-2985-2008.

Rinaldi, M., and Coauthors, 2010: Primary and secondary organic marine aerosol and oceanic biological activity: Recent results and new perspectives for future studies. *Adv. Meteor.*, **2010**, 310682, https://doi.org/10.1155/2010/310682.

Rolph, G., A. Stein, and B. Stunder, 2017: Real-Time Environmental Applications and Display System: READY. *Environ. Modell. Software*, **95**, 210–228, https://doi.org/10.1016/j.envsoft.2017.06.025.

Russell, L. M., D. H. Lenschow, K. K. Laursen, P. B. Krummel, S. T. Siems, A. R. Bandy, D. C. Thornton, and T. S. Bates, 1998: Bidirectional mixing in an ACE 1 marine boundary layer overlain by a second turbulent layer. *J. Geophys. Res.*, **103**, 16 411–16 432, https://doi.org/10.1029/97JD03437.

Sanchez, K. J., and Coauthors, 2018: Substantial seasonal contribution of observed biogenic sulfate particles to cloud condensation nuclei. *Sci. Rep.*, **8**, 3235, https://doi.org/10.1038/s41598-018-21590-9.

——, and Coauthors, 2021: Measurement report: Cloud processes and the transport of biological emissions affect southern ocean particle and cloud condensation nuclei concentrations, *Atmos. Chem. Phys.*, **21**, 3427–3446, https://doi.org/10.5194/acp-21-3427-2021.

Sato, K., J. Inoue, S. P. Alexander, G. McFarquhar, and Y. Yamazaki, 2018: Improved reanalysis and prediction of atmospheric fields over the Southern Ocean using campaign-based radiosonde observations. *Geophys. Res. Lett.*, **45**, 11 406–11 413, https://doi.org/10.1029/2018GL079037.

Schmale, J., and Coauthors, 2019: Overview of the Antarctic Circumnavigation Expedition: Study of Preindustrial-Like Aerosols and Their Climate Effects (ACE-SPACE). *Bull. Amer. Meteor. Soc.*, **100**, 2260–2283, https://doi.org/10.1175/BAMS-D-18-0187.1.

Sciare, J., O. Favez, R. Sarda-Estève, K. Oikonomou, H. Cachier, and V. Kazan, 2009: Long-term observations of carbonaceous aerosols in the Austral Ocean

atmosphere: Evidence of a biogenic marine organic source. *J. Geophys. Res.*, **114**, D15302, https://doi.org/10.1029/2009JD011998.

Scott, E. L., 2019: The influence of primary nucleation and rime splintering on ice number concentrations in Southern Ocean cumuli. M.S. thesis, Dept. of Atmospheric Sciences, University of Illinois at Urbana–Champaign, 104 pp.

Skamarock, W. C., J. B. Klemp, J. Dudhia, D. O. Gill, D. M. Barker, W. Wang, and J. G. Powers, 2005: A description of the Advanced Research WRF version 2. NCAR Tech. Note NCAR/TN-468+STR, 88 pp., http://dx.doi.org/10.5065/D6DZ069T.

Skofronick-Jackson, G., and Coauthors, 2017: The Global Precipitation Measurement (GPM) mission for science and society. *Bull. Amer. Meteor. Soc.*, **98**, 1679–1695, https://doi.org/10.1175/BAMS-D-15-00306.1.

Stein, A. F., R. R. Draxler, G. D. Rolph, B. J. B. Stunder, M. D. Cohen, and F. Ngan, 2015: NOAA's HYSPLIT atmospheric transport and dispersion modeling system. *Bull. Amer. Meteor. Soc.*, **96**, 2059–2077, https://doi.org/10.1175/BAMS-D-14-00110.1.

Stephens, B., and Coauthors, 2018: The O2/N2 ratio and CO2 Airborne Southern Ocean study. *Bull. Amer. Meteor. Soc.*, **99**, 381–402, https://doi.org/10.1175/BAMS-D-16-0206.1.

Tan, I., T. Storelvmo, and M. D. Zelinka, 2016: Observational constraints on mixed-phase clouds imply higher climate sensitivity. *Science*, **352**, 224–227, https://doi.org/10.1126/science.aad5300.

Toprak, E., and M. Schnaiter, 2013: Fluorescent biological aerosol particles measured with the Waveband Integrated Bioaerosol Sensor WIBS-4: Laboratory tests combined with a one year field study. *Atmos. Chem. Phys.*, **13**, 225–243, https://doi.org/10.5194/acp-13-225-2013.

Trenberth, K. E., and J. T. Fasullo, 2010: Simulation of present-day and twenty-first-century energy budgets of the southern oceans. *J. Climate*, **23**, 440–454, https://doi.org/10.1175/2009JCLI3152.1.

Truong, S. C. H., Y. Huang, F. Lang, M. Messmer, I. Simmonds, S. T. Siems, and M. J. Manton, 2020: A climatology of the marine atmospheric boundary layer over the Southern Ocean from four field campaigns. *J. Geophys. Res. Atmos.*, **125**, e2020JD033214, https://doi.org/10.1029/2020JD033214.

Twohy, C. H., and J. R. Anderson, 2008: Droplet nuclei in non-precipitating clouds: Composition and size matter. *Environ. Res. Lett.*, **3**, 045002, https://doi.org/10.1088/1748-9326/3/4/045002.

——, and Coauthors, 2021: Cloud-nucleating particles over the Southern Ocean in a changing climate. *Earth's Future*, **9**, https://doi.org/10.1029/2020EF001673.

Uetake, J., T. C. J. Hill, K. A. Moore, P. J. DeMott, A. Protat, and S. M. Kreidenweis, 2020: Airborne bacteria confirm the pristine nature of the Southern Ocean boundary layer. *Proc. Natl. Acad. Sci.*, **117**, 13 275–13 282, https://doi.org/10.1073/pnas.2000134117.

Vergara-Temprado, J., and Coauthors, 2018: Strong control of Southern Ocean cloud reflectivity by ice-nucleating particles. *Proc. Natl. Acad. Sci. USA*, **115**, 2687–2692, https://doi.org/10.1073/pnas.1721627115.

Vignon, É., and Coauthors, 2021: Challenging and improving the simulation of mid-level mixed-phase clouds over the highlatitude Southern Ocean. *J. Geophys. Res. Atmos.*, **126**, e2020JD033490, https://doi.org/10.1029/2020JD033490.

Wang, Y., and Coauthors, 2020: Microphysical properties of generating cells over the Southern Ocean: Results from SOCRATES. *J. Geophys. Res. Atmos.*, **125**, e2019JD032237, https://doi.org/10.1029/2019JD032237.

Wang, Z., S. T. Siems, D. Belusic, M. J. Manton, and Y. Huang, 2015: A climatology of the precipitation over the Southern Ocean as observed at Macquarie Island. *J. Appl. Meteor. Climatol.*, **54**, 2321–2337, https://doi.org/10.1175/JAMC-D-14-0211.1.

Warren, D. R., and J. H. Seinfeld, 1985: Prediction of aerosol concentrations resulting from a burst of nucleation. *J. Colloid Interface Sci.*, **105**, 136–142, https://doi.org/10.1016/0021-9797(85)90356-X.

Weber, R. J., and Coauthors, 1998: A study of new particle formation and growth involving biogenic and trace gas species measured during ACE 1. *J. Geophys. Res.*, **103**, 16 385–16 396, https://doi.org/10.1029/97JD02465.

Welti, A., and Coauthors, 2020: Ship-based measurements of ice nuclei concentrations over the Arctic, Atlantic, Pacific and Southern Oceans. *Atmos. Chem. Phys.*, **20**, 15 191–15 206, https://doi.org/10.5194/acp-20-15191-2020.

Wofsy, S. C., and Coauthors, 2011: HIAPER Pole-to-Pole Observations (HIPPO): Fine-grained, global-scale measurements of climatically important atmospheric gases and aerosols. *Philos. Trans. Roy. Soc.*, **369A**, 2073–2086, https://doi.org/10.1098/rsta.2010.0313.

Wolters, E. L. A., H. M. Deneke, B. J. J. M. van den Hurk, J. F. Merink, and R. A. Roebeling, 2010: Broken and inhomogeneous cloud impact on satellite cloud particle effective radius and cloud-phase retrievals. *J. Geophys. Res.*, **115**, D10214, https://doi.org/10.1029/2009JD012205.

Wu, C., X. Liu, M. Diao, K. Zhang, A. Gettelman, Z. Lu, J. E. Penner, and Z. Lin, 2017: Direct comparisons of ice cloud macro- and microphysical properties simulated by the Community Atmosphere Model version 5 with HIPPO aircraft observations. *Atmos. Chem. Phys.*, **17**, 4731–4749, https://doi.org/10.5194/acp-17-4731-2017.

Zeng, S., C. Cornet, F. Parol, J. Riedi, and F. Thieuleux, 2012: A better understanding of cloud optical thickness derived from the passive sensors MODIS/Aqua and POLDER/PARASOL in the A-Train constellation. *Atmos. Chem. Phys.*, **12**, 11 245–11 259, https://doi.org/10.5194/acp-12-11245-2012.

Zhang, X., S. Liang, G. Wang, Y. Yao, B. Jiang, and J. Cheng, 2016: Evaluation of the reanalysis surface incident shortwave radiation products from NCEP, ECMWF, GSFC, and JMA using satellite and surface observations. *Remote Sens.*, **8**, 225, https://doi.org/10.3390/rs8030225.

Zhang, X. L., P. Massoli, P. K. Quinn, T. S. Bates, and C. D. Cappa, 2014: Hygroscopic growth of submicron and supermicron aerosols in the marine boundary layer. *J. Geophys. Res. Atmos.*, **119**, 8384–8399, https://doi.org/10.1002/2013JD021213.

Zhao, M., and Coauthors, 2018: The GFDL global atmosphere and land model AM4.0/LM4.0: Simulation characteristics with prescribed SSTs. *J. Adv. Model. Earth Syst.*, **10**, 691–734, https://doi.org/10.1002/2017MS001208.

Zhou, X., R. Atlas, I. L. McCoy, C. S. Bretherton, C. Bardeen, A. Gettelman, P. Lin, and Y. Ming, 2021: Evaluation of cloud and precipitation simulations in CAM6 and AM4 using observations over the Southern Ocean. *Earth Space Sci.*, **8**, e2020EA001241, https://doi.org/10.1029/2020EA001241.